

Resolving the fine-scale velocity structure of continental hyperextension at the Deep Galicia Margin using full-waveform inversion

Davy, R.G.; Morgan, J.V.; Minshull, T.A.; Bayrakci, G.; Bull, J.M.; Klaeschen, D.; Reston, T.J.; Sawyer, D.S.; Lymer, G.; Cresswell, D.

DOI:

[10.1093/gji/ggx415](https://doi.org/10.1093/gji/ggx415)

[10.1093/gji/ggx415](https://doi.org/10.1093/gji/ggx415)

License:

Other (please specify with Rights Statement)

Document Version

Peer reviewed version

Citation for published version (Harvard):

Davy, RG, Morgan, JV, Minshull, TA, Bayrakci, G, Bull, JM, Klaeschen, D, Reston, TJ, Sawyer, DS, Lymer, G & Cresswell, D 2018, 'Resolving the fine-scale velocity structure of continental hyperextension at the Deep Galicia Margin using full-waveform inversion: Fine-scale velocity structure at Deep Galicia Margin', *Geophysical Journal International*, vol. 212, no. 1, pp. 244-263. <https://doi.org/10.1093/gji/ggx415>, <https://doi.org/10.1093/gji/ggx415>

[Link to publication on Research at Birmingham portal](#)

Publisher Rights Statement:

Checked for eligibility: 28/02/2018

This is a pre-copyedited, author-produced PDF of an article accepted for publication in *Geophysical Journal International* following peer review. The version of record

R G Davy, J V Morgan, T A Minshull, G Bayrakci, J M Bull, D Klaeschen, T J Reston, D S Sawyer, G Lymer, D Cresswell; Resolving the fine-scale velocity structure of continental hyperextension at the Deep Galicia Margin using full-waveform inversion, *Geophysical Journal International*, Volume 212, Issue 1, 1 January 2018, Pages 244–263, <https://doi.org/10.1093/gji/ggx415>

is available online at:

<https://academic.oup.com/gji/article/212/1/244/4331637>

General rights

Unless a licence is specified above, all rights (including copyright and moral rights) in this document are retained by the authors and/or the copyright holders. The express permission of the copyright holder must be obtained for any use of this material other than for purposes permitted by law.

- Users may freely distribute the URL that is used to identify this publication.
- Users may download and/or print one copy of the publication from the University of Birmingham research portal for the purpose of private study or non-commercial research.
- User may use extracts from the document in line with the concept of 'fair dealing' under the Copyright, Designs and Patents Act 1988 (?)
- Users may not further distribute the material nor use it for the purposes of commercial gain.

Where a licence is displayed above, please note the terms and conditions of the licence govern your use of this document.

When citing, please reference the published version.

Take down policy

While the University of Birmingham exercises care and attention in making items available there are rare occasions when an item has been uploaded in error or has been deemed to be commercially or otherwise sensitive.

If you believe that this is the case for this document, please contact UBIRA@lists.bham.ac.uk providing details and we will remove access to the work immediately and investigate.

1 **Resolving the fine-scale velocity structure of continental hyperextension at the**
2 **Deep Galicia Margin using full-waveform inversion**

3 R. G. Davy¹, J. V. Morgan², T. A. Minshull¹, G. Bayrakci¹, J. M. Bull¹, D. Klaeschen³,
4 T. J. Reston⁴, D. S. Sawyer⁵, G. Lymer⁴, D. Cresswell⁴.

5 1. University of Southampton, Southampton, United Kingdom.

6 2. Imperial College London, London, United Kingdom.

7 3. GEOMAR Helmholtz Centre for Ocean Research, Kiel, Germany.

8 4. University of Birmingham, Birmingham, United Kingdom.

9 5. RICE University, Houston, TX, United States of America.

10 **Abbreviated title:** Fine-scale velocity structure at Deep Galicia Margin

11 **Corresponding author:** Richard Davy, R.G.Davy@soton.ac.uk, +44 (0) 7783404703

12 **Summary**

13 Continental hyperextension during magma-poor rifting at the Deep Galicia Margin is
14 characterised by a complex pattern of faulting, thin continental fault blocks, and the
15 serpentinisation, with local exhumation, of mantle peridotites along the S-reflector,
16 interpreted as a detachment surface. In order to understand fully the evolution of these
17 features, it is important to image seismically the structure and to model the velocity structure
18 to the greatest resolution possible. Travel-time tomography models have revealed the long-
19 wavelength velocity structure of this hyperextended domain, but are often insufficient to
20 match accurately the short-wavelength structure observed in reflection seismic imaging. Here
21 we demonstrate the application of two-dimensional (2D) time-domain acoustic full-waveform
22 inversion to deep water seismic data collected at the Deep Galicia Margin, in order to attain a

23 high resolution velocity model of continental hyperextension. We have used several quality
24 assurance procedures to assess the velocity model, including comparison of the observed and
25 modelled waveforms, checkerboard tests, testing of parameter and inversion strategy, and
26 comparison with the migrated reflection image. Our final model exhibits an increase in the
27 resolution of subsurface velocities, with particular improvement observed in the westernmost
28 continental fault blocks, with a clear rotation of the velocity field to match steeply dipping
29 reflectors. Across the S-reflector there is a sharpening in the velocity contrast, with lower
30 velocities beneath S indicative of preferential mantle serpentinisation. This study supports the
31 hypothesis that normal faulting acts to hydrate the upper mantle peridotite, observed as a
32 systematic decrease in seismic velocities, consistent with increased serpentinisation. Our
33 results confirm the feasibility of applying the full-waveform inversion method to sparse, deep
34 water crustal datasets.

35 **Keywords:** Controlled source seismology, Waveform inversion, Seismic tomography,
36 Continental margins: divergent; Crustal structure; Fractures, faults, and high strain
37 deformation zones.

38 **1. Introduction**

39 In recent years there has been an increase in the availability of high-density seismic datasets
40 and a significant increase in the power of computers. These combined factors have enabled a
41 broadening application of seismic full-waveform inversion (FWI). FWI provides a powerful
42 extension of popular seismic travel-time tomography methods, with the ability to resolve
43 subsurface velocity structure to half the seismic wavelength, which can be an order of
44 magnitude smaller than possible with travel-time tomography for a typical crustal target (Wu
45 and Toksöz 1987; Williamson 1991; Virieux and Operto 2009). Three-dimensional FWI has
46 yielded impressive results on marine seismic datasets, producing high resolution velocity

47 models which can be used directly for geological interpretation or for the migration of
48 reflection seismic data to produce detailed images (e.g. Sirgue *et al.* 2010; Ratcliffe *et al.*
49 2011; Warner *et al.* 2013; Mispel *et al.* 2013; Jones *et al.* 2013; Mothi *et al.* 2013). The vast
50 majority of such studies have utilised seismic data recorded on either hydrophone streamers
51 or ocean bottom cables (OBC), in relatively shallow marine environments (water depth
52 < 1,000 m). Both hydrophone streamers and OBC possess a high density of receivers,
53 enabling dense sampling of the subsurface for the FWI process (Warner *et al.* 2013).
54 However, the maximum depth of investigation for these methods is restricted to
55 approximately a third to a sixth of the maximum source-receiver offset, limiting their use for
56 studies of crustal scale targets or those in deep water environments (Warner *et al.* 2010;
57 Morgan *et al.* 2013).

58 These limitations can be overcome in deep water environments by applying FWI to wide-
59 angle seismic datasets recorded by ocean bottom seismometers and hydrophones (OBS/H). A
60 limited number of studies have previously applied FWI to OBS/H datasets. Dessa *et al.*
61 (2004) and Operto *et al.* (2006) presented the first results of frequency-domain FWI applied
62 to OBS data, utilising a 2D deployment of 100 instruments at the Nankai Trough, east of
63 Japan. The velocity structure of compressional tectonic features within the accretionary prism
64 and the down going oceanic crust were resolved, where they had not previously been
65 observed in travel-time tomographic models. Kamei *et al.* (2012) applied frequency-domain
66 FWI to a separate deployment of 54 OBS at the Nankai trough, resolving the fine scale
67 velocity structure of megasplay faulting. Recently, Morgan *et al.* (2016) demonstrated the
68 application of three-dimensional (3D) time-domain FWI on an array of 21 OBS situated
69 across the Endeavour oceanic spreading centre of the Juan de Fuca Ridge, revealing low-
70 velocity zones interpreted to represent a magmatic-hydrothermal reaction zone (Arnoux *et al.*
71 2017). These studies have made use of relatively dense OBS deployments (~ 1 km spacing),

72 or a 3D seismic shooting configuration, both of which are not always possible in academic
73 experiments. We build on these studies by applying FWI to a comparatively sparse dataset
74 (sparse OBS locations recording frequent seismic shots), in order to demonstrate the
75 feasibility of the technique in areas where only 2D or older datasets are available.

76 Here we demonstrate the application of acoustic 2D FWI to a sparse wide-angle dataset
77 collected on 19 OBS/H at the Deep Galicia Margin in the North Atlantic, with the aim of
78 resolving the fine-scale velocity structure of continental hyperextension. Continental fault
79 blocks within this hyperextended domain can possess dimensions as small as a few
80 kilometres, beyond the limit of what is resolvable with travel-time tomography, making this
81 an ideal target for FWI (Davy *et al.* 2016). We investigate the robustness of our FWI result
82 by testing several parameters influencing the inversion, including the offsets and time
83 windowing of the input data, and uncertainties in the sediment velocity model. Our result
84 cannot be quality checked using 3D phase plots, and so we utilise alternative quality
85 assurances, including checkerboard tests, waveform comparisons, and correlation with
86 reflection seismic imaging. Given the nature of both the dataset and our crustal target, this
87 application of FWI provides an excellent case study to explore the practical limits of this
88 increasingly popular technique.

89 **2. Background**

90 **2.1 Geologic setting**

91 Rifting at the Deep Galicia Margin (Fig. 1A) has resulted in the extreme thinning of the
92 continental crust over distances of 100 – 200km. Unaltered crust landward of the proximal
93 rift margin is ~30 km thick and has been thinned through a complex pattern of faulting to
94 only a few km at the distal limits of the margin (Zelt *et al.* 2003; Reston 2009). Initial
95 extensional deformation is inferred to have occurred as high-angle normal faulting, which

96 formed large fault-bound blocks between 10 and 20 km wide, thinning the crust to between
97 20 and 30 km thick (Ranero and Pérez-Gussinyé 2010). With continued extension of the
98 margin, these continental fault blocks rotated to low-angles, at which point their bounding
99 faults locked up (Ranero and Pérez-Gussinyé 2010). The faulting mechanism responsible for
100 how continued extension was accommodated still remains controversial. McDermott and
101 Reston (2015) propose that the crust deformed through polyphase faulting, where new
102 preferentially oriented normal faults overprinted existing faults and fault blocks. Ranero and
103 Pérez-Gussinyé (2010) suggest that the continued deformation occurred as a sequential
104 pattern of faulting, where new preferentially oriented normal faults were successively formed
105 through the thinned crust, but did not cut the preceding fault. Both of these proposed
106 mechanisms lead to the extreme thinning of the continental crust.

107 As the margin extended and thinned at an ultra-slow rate (< 10 mm/yr half spreading rate), it
108 allowed time for the entire crust to cool conductively, resulting in the normally ductile mid-
109 and lower-crust becoming progressively embrittled (Srivastava *et al.* 2000; Pérez-Gussinyé
110 and Reston 2001; Pérez-Gussinyé *et al.* 2003). Once the crustal thicknesses reached < 10 km,
111 the entire crust became brittle and coupled, a phenomenon known as continental
112 hyperextension. A fully embrittled crust enabled normal faults to form through the entire
113 crust, from the seafloor to the underlying mantle (Pérez-Gussinyé and Reston 2001; Pérez-
114 Gussinyé *et al.* 2003; Pérez-Gussinyé 2013). These faults acted as conduits, delivering
115 seawater to the upper mantle and forming a layer of serpentinitised mantle, which is an
116 inherently weak material (Pérez-Gussinyé and Reston 2001; Reston *et al.* 2007; Bayrakci *et*
117 *al.* 2016). With continued extension these faults soled out into the structurally weak layer of
118 mantle serpentinite, forming a large and low angle ($< 20^{\circ}$) detachment fault, known as the
119 S-reflector (Fig. 1C), which also corresponds to the crust-mantle boundary in the distal
120 margin (Reston *et al.* 2007). It has been shown recently that these faults, which sole into the

121 S-reflector, preferentially hydrate the upper mantle which results in varying degrees of
122 mantle serpentinisation, observed as a pattern of high and low P-wave velocities (Bayrakci *et al.*
123 *et al.* 2016; Davy *et al.* 2016). In the final stages of rifting, serpentinised subcontinental mantle
124 was exhumed to the seafloor along the S-reflector, and was also emplaced west of this
125 hyperextended domain, forming a structure known as the Peridotite Ridge (Beslier *et al.*
126 1993), before the onset of seafloor spreading (Davy *et al.* 2016). Sedimentation of this
127 margin occurs at all stages of the rifting process, giving rise to pre-, syn- and post-rift
128 sedimentary units, which are mentioned throughout our interpretations (Fig. 1D) (Ranero and
129 Pérez-Gussinyé 2010).

130 **2.2 Seismic dataset**

131 This study investigates a 2D subset (3D inline 420) of the Galicia-3D seismic experiment,
132 which was performed at the Deep Galicia Margin, west of Spain (Fig. 1A) between 1 June
133 2013 and 2 August 2013 (Fig. 1B); (see Davy *et al.* (2016) and Dean *et al.* (2015) for further
134 details on the wide-angle and multichannel seismic survey parameters, respectively).
135 Multichannel seismic reflection data were recorded by the RV *Marcus G. Langseth* towing
136 four streamers of ~6 km length, spaced 200 m apart, and at a depth of 15 m. Each streamer
137 had 468 channels spaced at 12.5 m intervals. The seismic source comprised two 3,300 cu. in.
138 air gun arrays, towed at a depth of 9 m and fired alternately every 37.5 m (a shot interval of
139 ~16 s), optimal for high resolution 3D reflection imaging, but sub-optimal for wide-angle
140 studies. Processing of this reflection seismic dataset was performed by Repsol, who produced
141 a 3D pre-stack Kirchhoff time migration. Wide-angle seismic arrivals along this 2D profile
142 were recorded by 26 ocean-bottom seismometers and hydrophones (OBS/H) from the UK
143 Ocean Bottom Instrumentation Facility (OBIF) (Minshall *et al.* 2005) and GEOMAR (Fig.
144 1B). The eastern 17 OBS/H were spaced densely at ~1.7 km intervals, with the intention to
145 produce a high resolution 2D velocity models of the geologic structure above and below the

146 S-reflector and form the focus of this study. The western 9 OBS/H, spaced at distances of
147 ~3.4 km, cover the Peridotite Ridge (Fig 1C) and the sedimentary basins on its western and
148 eastern flanks. Two of the 26 OBS/H were not retrieved, while another five instruments
149 returned no usable data.

150 Most of the OBS/H in the Galicia-3D seismic experiment recorded seismic shots with a
151 complete azimuthal coverage, allowing these instruments to be accurately relocated by
152 minimising the travel-time misfit between the observed and calculated direct water wave
153 arrival. However, eight OBH along this line were deployed for a shorter period and only
154 recorded shots from a single seismic profile, limiting their ability to be relocated accurately in
155 the cross-line direction (OBH 79-86). On average each instrument was relocated by 299 m.

156 **3. Full waveform inversion**

157 The theory behind FWI and its application to seismic data was first developed in the 1980's
158 by Lailly (1983) and Tarantola (1984). It was shown that finite difference modelling of the
159 wavefield through a starting medium, followed by a localised least-squares inversion,
160 minimising the misfit between observed and modelled wavefield, could be used to recover
161 physical properties of the subsurface (Tarantola 1987). Initial applications of FWI were
162 performed in the time domain, but were limited given the high computational demand of the
163 method (Kolb *et al.* 1986). Three decades later and FWI is still performed based on these
164 underlying principles, with modern codes capable of performing FWI in either the time or
165 frequency domain, in two or three dimensions, approximating either the acoustic or elastic
166 wave equation, and can include the effects of seismic attenuation and anisotropy (e.g., Pratt
167 1999; Brossier *et al.* 2009; Warner *et al.* 2013). It has also been shown that the maximum
168 achievable resolution using these codes is on the order of half the seismic wavelength,
169 making it superior to travel-time tomography (Virieux and Operto 2009). Although FWI can

170 extract any physical property which affects the wave equation, it is most commonly used to
171 determine the compressional velocity structure of the subsurface (e.g. Kapoor *et al.* 2013).

172 FWI requires an accurate starting model (typically derived from reflection or travel-time
173 tomography) capable of reproducing the majority of the observed wavefield to within half a
174 seismic cycle at the lowest inversion frequency, observed seismic data, and a derivation of a
175 source wavelet (Virieux and Operto 2009). Forward modelling of synthetic wavefields
176 through the starting model is achieved by solving the numerical wave equation (either
177 acoustic or elastic) through a method of finite differences (Virieux 1986; Operto *et al.* 2007).

178 Residual data are then calculated as the difference between the synthetic and observed data,
179 and then the residuals are back propagated through the velocity model and subsequently
180 cross-correlated with the synthetic data to determine a model update (Tarantola 1984; Pratt *et*
181 *al.* 1998; Virieux and Operto 2009). Iteration of this process builds an increasingly resolved
182 velocity model, capable of reproducing the observed wavefield to greater degree. As FWI is a
183 localised inversion method it runs the risk of converging to a local minimum, commonly
184 referred to as cycle-skipping (Bunks *et al.* 1995; Sirgue 2006). Cycle-skipping occurs when
185 seismic arrivals in the synthetic wavefield are more than 180° out of phase with that of the
186 observed wavefield. This results in the inversion process attempting to force a match between
187 the observed and synthetic wavefield which is one or more cycles from the true match. In an
188 effort to mitigate against cycle-skipping, it is common practice to start FWI at long
189 wavelengths (low frequencies), which are easier to match within half a cycle, and
190 systematically incorporate shorter wavelengths (higher frequencies) into the modelling,
191 commonly referred to as multiscale FWI (Bunks *et al.* 1995; Sirgue 2006). A complete
192 description of FWI and the underlying theory can be found in Pratt *et al.* (1998) and the
193 review paper of Virieux and Operto (2009).

194 In this study we perform a 2D time-domain, acoustic, isotropic FWI, using the codes of
195 Warner *et al.* (2013). In this code, synthetic traces are calculated through a starting model
196 using a finite difference method and are subsequently scaled so that their RMS amplitude
197 matches that of their corresponding observed trace. Misfit between the respective synthetic
198 and observed traces is calculated as the sum of squares difference for each time interval, with
199 a misfit functional representing the misfit over all traces. As this is a time-domain code, the
200 inversion process matches a finite bandwidth of the observed wavefield, defined by a low-
201 pass filter in which the maximum frequency is progressively increased during the inversion.
202 At each bandwidth the misfit functional was minimised by an iterative gradient-based
203 optimisation, which perturbed an input velocity model in order to match the calculated
204 synthetic and respective observed traces, based on the phase shape and relative amplitude of
205 individual arrivals. The code maintains a deterministic relationship between velocity and
206 density, using Gardner's law below the seafloor (Gardner *et al.* 1974).

207 **3.1 Data pre-processing and derivation of the source wavelet**

208 A mixture of four-component ocean-bottom seismometers and single component ocean-
209 bottom hydrophones were utilised in this study; the FWI was performed on the hydrophone
210 channel which was present for all instruments and yielded the highest signal-to-noise ratio.
211 Spectral analysis of the hydrophone data showed that there is a reasonable signal-to-noise
212 ratio at frequencies down to ~ 3.0 Hz. As we wanted to match the modelled wavefield to the
213 observed wavefield, without cycle skipping, we included signal at the lowest frequencies
214 possible. A minimum phase Ormsby band-pass filter with corner frequencies of 2.0, 3.0, 4.5
215 and 6.5 Hz was applied to the hydrophone data in order to isolate the low-frequency signal
216 from unwanted noise (Fig. 2A). Typical data pre-processing for the purpose of FWI may look
217 to maintain the lower frequency data by simply applying a low-pass filter, but we needed also
218 to diminish the effects of coherent low-frequency noise from the previous seismic shot. A top

219 mute was applied ~ 0.1 s before the first seismic arrival, in order to remove the noisy water
220 column, and a bottom mute was applied 1.8 s after this top mute (Fig. 2B) in order to include
221 the first-arriving wavefield which, at these frequencies, is about 1.0 - 1.5 s in length (Fig.
222 2A). This muting process creates a time window for the input field data which incorporates
223 the direct water arrival and refractions through the crust (Pg) and upper mantle (Pn) (Fig.
224 2B).

225 We use a free surface to represent the reflective sea surface, so, we use a deghosted source
226 wavelet to generate synthetic data for FWI. The deghosted source wavelet is obtained using a
227 Weiner matching filter and here, we used the following steps: 1) guessing a source wavelet
228 by selecting a clear noise-free near-offset direct water-wave arrival into an OBS (OBS46 was
229 selected), windowing this arrival by 1 s, and applying an identical bandpass filter to this
230 guessed source wavelet and field data (Ormsby band-pass filter with corner frequencies of
231 2.0,3.0, 4.5and 6.5 H); 2) generating a synthetic water-wave arrival for the selected OBS
232 using the guessed band-pass filtered source wavelet and starting model; 3) finding the inverse
233 filter that matches this synthetic trace to the observed trace; and 4) applying this inverse filter
234 to the initial source guess to generate the new source wavelet. This new source was then used
235 to generate the nearest-offset direct wave through the water for all OBS and compared to the
236 equivalent observed arrival (Fig. 3). The excellent match between the observed and synthetic
237 data shows that this source wavelet is appropriate for all the OBS. The similarity of the
238 waveforms for all OBS indicates that there is no significant change in the source wavelet
239 during the survey, and that there are no significant differences in the OBS response at the
240 frequencies used in the inversion.

241 **3.2 Starting model**

242 The starting model for the FWI process is a modified version of the 2D compressional
243 seismic travel-time tomography model described by Davy *et al.* (2016). This model was
244 developed using OBS data collected from the Galicia-3D seismic experiment, supplemented
245 with data from the ISE-1 seismic profile (Sawyer *et al.* 1997; Zelt *et al.* 2003), and inverted
246 using the “TOMO2D” travel-time inversion code of Korenaga *et al.* (2000). The final
247 TOMO2D model has an overall travel-time misfit of 53 ms, and a chi-squared value of 0.97.
248 We shortened this model to include only the easternmost 68 km of the seismic profile where
249 the OBS are more closely spaced, to a depth of 12 km, and defined the model on a grid with a
250 horizontal and vertical spacing of 50 m. FWI requires 4 - 5 model nodes per seismic
251 wavelength (Warner *et al.* 2013), and so with water velocities of $\sim 1.5 \text{ km s}^{-1}$ a node spacing
252 of 50 m allows inversion frequencies of up to 6.0 - 7.5 Hz. In the TOMO2D analysis, a
253 constant velocity of 1.52 km s^{-1} was used for the water column. This is sufficient for travel-
254 time tomography, but not for reproducing consistently the first seismic arrivals to within half
255 a cycle of those observed in the field data. Sound velocity profiles, used for the processing of
256 the multibeam bathymetry collected during the survey, were used in place of this constant
257 velocity approximation. The resulting model gives an accurate fit of the direct arriving
258 waveforms through the water-column (12.7 ms for all instruments, on average), as shown in
259 Fig. 3.

260 Sediment velocities in this starting model were determined by the forward modelling of a
261 prominent sedimentary reflector and very limited sediment refractions, and are therefore
262 relatively unconstrained. This is the result of the large crossover distance between the direct
263 water wave and the refracted arrivals from the subsurface, dictated by the depth of the
264 instrument deployment. The effect of uncertainty in sediment velocities on the final FWI
265 velocity model is examined later in the paper.

266 The velocity model was smoothed in both the horizontal and vertical directions in order to
267 remove any features that have a shorter wavelength than obtainable by FWI at the lowest
268 inversion frequency. A 2D convolution filter, using 3 samples in the vertical direction (150
269 m) and 9 samples in the horizontal direction (450 m), was used for this smoothing process.
270 Our starting model can be seen in Fig. 4A.

271 **3.3 Data selection**

272 Using this starting velocity model, synthetic receiver gathers were produced with the same
273 source-receiver geometry as the original seismic experiment (Fig. 2C). Synthetic gathers
274 were used as a quality control for the field data to be input into the FWI process. Of the 20
275 instruments which yielded useable data, one was rejected for being too noisy. The final
276 instrument coverage used for the FWI is shown in Fig. 1B.

277 Within the offset range between 0 m and 5,000 m the first arrivals comprise direct water
278 waves and sub-horizontally travelling turning waves which sparsely sample the shallow sub
279 seafloor (Fig. 2B). When included in the inversion these arrivals tend to dominate due to their
280 large amplitudes, and the inversion attempts to match changes in waveform structure by
281 introducing rapid changes in shallow sub-seafloor velocities which are poorly constrained. Pg
282 and Pn arrivals travel sub-vertically through the shallow section below each OBS, and
283 therefore pass relatively rapidly through this region, so their travel-times will not be
284 significantly affected by the shallow velocity structure. Thus, it was decided to exclude this
285 offset range (0 – 5000 m) from the inversion, and not attempt to resolve velocity in the
286 shallow sub seafloor, which is a region of low scientific interest.

287 We assessed the data from each individual instrument to identify the maximum offsets to
288 which the first seismic arrival could be positively identified and matched to the synthetic
289 wavefields to within half a seismic cycle. Travel-time picks from Davy *et al.* (2016) were

290 used as guidance in this process. These maximum offsets were then used as the upper bounds
291 for data input for the respective instrument. Maximum input data offsets ranged from 13.0 to
292 23.0 km across the 19 instruments utilised in the inversion (Fig. 2B shows maximum data
293 offsets used for OBS 46).

294 **3.4 Inversion**

295 We assumed an isotropic medium for the inversion, based on previous joint reflection and
296 refraction travel-time tomography (Davy *et al.* 2016). These joint inversions resolved the
297 S-reflector by constraining the velocity field using refraction data and determining the
298 reflector depth using wide-angle reflections. These results showed an excellent match to the
299 S-reflector resolved in reflection imaging, where ray-paths are near vertical. This observation
300 indicates that any anisotropy is quite weak, justifying our assumption of isotropy.

301 We developed the inversion by increasing progressively the cut-off frequency of the low pass
302 filter applied to the input data, which was set at 3.0, 3.4, 3.9, 4.5 and 5.2 Hz (Fig. 4).
303 Velocities of below 2.0 km s^{-1} in the starting model were kept constant during the inversion
304 to keep the water velocity and sea bottom fixed, since these parameters had been determined
305 independently, and were confirmed by synthetic direct water waves through the starting
306 model (Fig. 3). Velocities were not allowed to be updated above 8.50 km s^{-1} as this was
307 considered to be the maximum realistic value for the uppermost mantle here. The inversion
308 process was iterated 10 times for each filter setting, with the resulting velocity model acting
309 as the input to the next inversion iteration (Fig. 4). After 10 inversion iterations at each
310 bandwidth the reduction in the model misfit was less than 0.5% of the previous inversion
311 iteration, which we believed to be a sufficient convergence (Fig. 5). Relatively small
312 reductions in the misfit functional were seen for each inversion frequency, see Table 1.

313 The complete inversion process runs through 50 iterations to produce the final inversion
314 model (Fig. 4F). Systematically introducing higher frequencies of input data into the
315 inversion process gradually increases the resolution of the resulting velocity model (Fig. 4A-
316 F).

317 Testing of the inversion parameters included examining the effects of: the maximum data
318 offsets used, the length of the time window around the first seismic arrival, and uncertainty in
319 the sediment velocities in the starting model. The results of these parameter tests were
320 checked against reflection seismic images, and the observed field data, in order to make
321 informed decisions on the best parameterisation. The next three subsections describe the
322 results of these tests.

323

324 **3.5 Data offsets**

325 One of the limitations of this dataset is the range of useable data offsets. Given the deep-
326 water setting, Pg refractions only become first arrivals at offsets of > 5,000 m, reducing our
327 ability to resolve shallow subsurface structure. At longer offsets (> ~12,000 m) the data
328 become adversely affected by coherent noise from the third multiple (and higher order
329 multiples) of the previous seismic shots (Fig. 2A). This is problematic because the crustal
330 targets (fault rotated continental blocks, the S-reflector and uppermost mantle) are up to
331 5,000 m below the seafloor, but we can only expect to resolve targets at depths approximately
332 between a sixth and third of the maximum source-receiver offset (Warner *et al.* 2010;
333 Morgan *et al.* 2013). This means that our inversion model, for data offsets > 12,000 m, may
334 be prone to noise-induced artefacts when attempting to resolve structure at depths greater
335 than 2,000 – 4,000 m below the seafloor. To test whether our selected maximum data offsets
336 (between 13.0 and 23.0 km) produced a robust model, we tested arbitrary maximum data

337 offsets of 10, 15 and 20 km for all instruments used in the inversion. All other inversion
338 parameters were identical to those described in section 3.4. Fig. 6 shows the resulting models
339 and 1D profiles at set distances through each model.

340 When limiting input data offsets to 10 km (Fig. 6A), the resulting velocity model has many
341 closed velocity contours, high lateral and depth variability, and features which would be
342 described as non-geologic. This is expected given the sparse coverage and relatively shallow
343 depth of penetration when offsets are limited to 5 to 10 km, as waves are expected to only
344 travel to depths of 1.6 – 3.3 km below the seafloor. It can be seen in the 1D plots (Fig. 6E-J)
345 that the model utilising 10 km data offsets has a good correlation with the trends of the other
346 models to depths of ~ 1.2 – 3.0 km below the seafloor, as would be expected. The only
347 exception to this is at ~ 40 km profile distance (Fig. 6H). Below these depths, the 10 km
348 offset model varies from the other models by up to 1.38 km s^{-1} (e.g. 3.0 km below the
349 seafloor at 50 km profile distance), because the model is unconstrained at these depths.

350 The remaining three models share common features and velocity values. These models
351 appear much smoother than that produced using data offsets from 5 to 10 km. The 1-D
352 velocity profiles confirm that the models have common trends with depth, throughout the
353 model (Fig. 6E-J), but we observe that the model utilising offsets of 15 km deviates from our
354 final inversion model and that using maximum offsets of 20 km, at depths greater than 4 km
355 below the seafloor on profiles at 10, 30 and 50 km. Again, these deviations are unsurprising
356 given that the expected depth of penetration when using maximum offsets of 15 km is up to
357 2.5 – 5.0 km.

358 This similarity, especially between models using 15 and 20 km offset of input data, indicates
359 that incorporating data with coherent noise yields results which are comparable to those

360 inversions which exclude noisy data altogether. These results also suggest that the FWI is
361 relatively insensitive to noise.

362 **3.6 Data windowing**

363 Data input into the inversion process were top and bottom muted, allowing a 1.8 s window of
364 data to be matched in the inversion process. This time window was determined heuristically
365 in order to include only the primary compressional seismic phase arrivals (i.e. Pg and Pn,
366 Fig. 2A), while excluding mode-converted later arrivals, which cannot be reproduced by the
367 acoustic wave approximation (Jaiswal *et al.* 2008). Windows of 1.8 s were selected, based on
368 inspection of the length of the band passed first-arriving waveform (Fig. 2A). To investigate
369 the effect of the data window length, the inversion process was run also with data windows of
370 lengths 1.0, 1.5, 2.0 and 2.5 s (Fig. 7). It appears that longer window lengths introduced more
371 complicated structure to the resulting velocity model, a result of the inversion process trying
372 to fit the later parts of the seismic coda and later arrivals. A time window of 2.5 s resulted in a
373 rough model with a significant number of closed velocity contours, which are geologically
374 unlikely for this setting. Conversely, a time window of 1.0 s resulted in a smooth model,
375 which is geologically reasonable, but failed to match reflections in the seismic images as well
376 as inversion model using a time window of 1.8 s. We also observed a significant decrease in
377 seismic velocity in the resolved upper mantle in the central section of the profile, with an
378 increasing window length (depths of 9.0 – 10.5 km, 25.0 – 32.0 km profile distance, Fig. 7C-
379 D; deeper than 4.0 km below seafloor in Fig. 7G). Despite these differences, the overall
380 velocity structure observed in the plots and the trends of the 1D velocity profiles, remained
381 relatively constant. Consistency in the resulting FWI models and the observed depth-velocity
382 profiles, when using time windows of 1.0, 1.5 and 2.0 s for FWI, indicates that our chosen
383 time window of 1.8 s is appropriate.

384 3.7 Sedimentary velocities

385 As mentioned earlier in this section, the post-rift sediment velocities in the starting model
386 were poorly constrained, so we test the effects of varying post-rift sedimentary velocities in
387 the starting model. In the original model, the post-rift sediments were defined by two discrete
388 sedimentary layers; the top has velocities increasing from 2.00 to 2.15 km s⁻¹, while the
389 bottom layer has velocities increasing from 2.30 to 2.60 km s⁻¹. These layers were
390 constrained by inter-sedimentary reflectors (at offsets < 5,000 m) and limited sedimentary
391 refractions (at offsets > 5,000 m). To test the uncertainty in sedimentary velocities in our
392 starting model, we performed the TOMO2D travel-time inversion of Davy *et al.* (2016) with
393 starting models possessing low sediment velocities (1.80 – 2.00 km s⁻¹), high sediment
394 velocities (2.60 – 3.00 km s⁻¹), a low-velocity gradient (2.30 – 2.50 km s⁻¹) and a high-
395 velocity gradient (1.80 – 3.20 km s⁻¹). All travel-time inversion parameters remained identical
396 to that described in Davy *et al.* (2016). The outputs of these travel-time inversions were then
397 used as the starting models for the FWI process, with the inversion results observable in Fig.
398 8. With the exception of the low sediment velocity model, the general velocity structure
399 below the post-rift sediments remains consistent. Where post-rift sediment velocities are low,
400 higher velocities are observed directly below the top of the syn-rift sediments, and vice-versa
401 where the post-rift sediment velocities are high. This behaviour is a result of both the travel-
402 time tomography and FWI. The phenomenon is amplified in areas of thicker post-rift
403 sediment (i.e.: at 10, 20 and 50 km profile distance). For example, at 50 km profile distance
404 the difference between the low and high sediment velocity models is 1.75 km s⁻¹ at 1.65 km
405 below the base of the post-rift sediment (Fig. 8I). This result indicates that variations in the
406 starting post-rift sedimentary velocities are compensated for by the velocities below the post-
407 rift sediment, in order for the total travel-times to fit. Along the representative depth-velocity
408 profiles (i.e.: 10, 20, 30, 40, 50 and 60 km profile distance), the depth-averaged range of

409 velocities recovered for the range of starting models, excluding the low-velocity post-rift
410 sediment velocity model, is 0.12 km s^{-1} . We conclude that, since the sediments are unlikely to
411 have such low velocities, the overall velocity structure of the inversion models below the
412 post-rift sediment are minimally affected by uncertainty in the postrift sedimentary velocities.

413 **3.8 Assessing the modelled wavefield**

414 One measure of the success of FWI is how accurately the observed wavefield is reproduced,
415 and this is done by comparison with the synthetic wavefield. Fig. 9 shows the propagation of
416 the source wavelet through the final inversion model to produce the synthetic wavefield. In
417 this example, we have reversed the source and receiver configuration and are treating the
418 OBS 46 as the seismic source, and the shot locations as receivers. This approach
419 demonstrates the interaction of the wavefield with subsurface structure, and how that results
420 in the observed wavefield. East of OBS 46, the wavefield refracts through significant
421 subsurface topography in the form of a rotated continental fault block, giving the travel-time
422 of the first seismic arrival significant lateral variability (arrow ii, Figure 2C). Conversely,
423 west of OBS 46, the top of the rotated continental fault block dips smoothly westward,
424 resulting in a first seismic arrival of little variation (arrow i, Figure 2C). These synthetically
425 produced travel-time features, resulting from the modelled subsurface topography, match
426 those in the observed wavefield (Fig. 2A-B).

427 In order to compare the match between the observed and modelled wavefields, we interleaved
428 traces from alternative offset bins of 200 m (i.e.: traces with instrument offsets between 200 –
429 400 m, 600 – 800 m, etc. are taken from the observed wavefield and are combined with traces
430 with instrument offsets between 0 – 200 m, 400 – 600 m, etc. from the synthetic wavefield)
431 (Figs 10-12A-B). Where the wavefields match, a continuous wavefield will be observed over
432 distances greater than the 200 m trace bins. Where the match is poor, a discontinuous

433 wavefield will be observed over such distances. Comparing the observed wavefield with the
434 synthetic wavefield through the starting model (Figs 10-12A), it can be seen that the direct
435 water arrival (-7.0 – 7.0 km) shows high continuity, indicating that the starting velocity
436 model has reasonably accurate water and sub-seafloor velocities. The wavefield appears to be
437 fairly consistent at some wider offsets, for example between -11 to -15 km on OBS 46 (Fig.
438 11A) and -10 to -14 on OBS 54 (Fig. 12A), indicating that the starting model at depth is close
439 to the true velocity structure in particular areas. There are also notable mismatches in the first
440 seismic arrivals, outside the direct water arrival, for example at offsets between -7 and -11
441 km and between 7 and 13 km on OBS 46 (Fig. 11A) and 6 to 10 km on OBS 37 (Fig. 10A),
442 which indicates that the velocities in sections of the thinned continental crust are not
443 reproducing the wavefield accurately. However, these mismatches appear to be less than half
444 a seismic cycle, which is a prerequisite to avoid cycle skipping during the FWI process.
445 Significant improvements in the match between wavefields are observed when comparing the
446 observed and synthetic wavefield through the FWI velocity model (Figs 10-12B). Areas
447 previously mismatched (for example between offsets of 7 – 13 km on OBS 46) now appear
448 more continuous (see arrows) indicating that the FWI process has modified the subsurface
449 velocities in such a way that the travel-time and phase of these synthetic waveforms match
450 those that are observed. Where the starting model already matched the observed wavefield
451 well there is little to no change, as would be expected.

452 Directly comparing traces at set offsets also shows how the synthetic waveforms are modified
453 through the FWI process. Figs 10C-H, 11C-G, and 12C-G, show trace-to-trace comparisons
454 of the observed wavefield and synthetic wavefield through the starting velocity model, while
455 Figs 10I-N, 11H-L, and 12H-L, show trace-to-trace comparisons of the observed wavefield
456 and synthetic wavefield through the final velocity model. Despite the small changes in the
457 inversion misfit (Fig. 5), we observe significant improvements in the synthetic wavefield. For

458 example, at offsets of -10.05, -7.52, 8.63 and 11.93 km on OBS 46 (Fig. 10D-G), the
459 synthetic traces through the starting model exhibit shapes close to the observed waveform,
460 but with amplitude differences and phase shifts within half a seismic cycle. After the FWI,
461 the synthetic traces have relative amplitudes and phases that match well the observed traces
462 (Fig. 10J-M), indicating that the new velocity model is a more accurate representation of the
463 subsurface. Observed traces at the furthest input offsets (i.e.: -14.92 and 16.80 km on OBS
464 46, 18.06 km on OBS 37, and -17.57 km on OBS 54, Figs 11I, 11N, 10L, and 12H,
465 respectively) are being affected by coherent noise, and FWI is struggling to match these more
466 complicated waveforms. It appears that the trace at -14.92 km on OBS 46 is cycle skipped in
467 the starting model, and although the inversion has led to an improvement in the shape of the
468 waveform it has not changed its travel-time, which should be earlier. The onset of reduced
469 performance of FWI at longer offsets reinforces the decision to limit the offsets of the input
470 data, based on visual inspection of the match between the observed data and synthetic data
471 from the starting model.

472 **3.9 Checkerboards**

473 The maximum achievable resolution of the final FWI velocity model was assessed by a series
474 of checkerboard tests (Zelt and Barton 1998). Alternating velocity perturbations of $\pm 2\%$
475 were introduced into the starting velocity model in checkerboard patterns to create reference
476 models with anomaly dimensions of 10.0 km x 2.0 km, 5.0 km x 1.0 km, and 2.5 km x 0.5
477 km (Fig. 13). Small velocity perturbations of $\pm 2\%$ are used in order to avoid major changes
478 in the modelled wave-paths, which could lead to the synthetic data generated from the
479 checkerboard and starting model being cycle skipped. Synthetic receiver gathers were then
480 produced through these reference models by forward modelling of the wavefield, using the
481 same shot-receiver geometry as the receiver gathers used in the FWI. These synthetic receiver
482 gathers were windowed and inverted with identical FWI parameters. The differences between

483 these inversion results and the unperturbed starting velocity model were used to determine
484 the length scale of structure resolvable in the final FWI model (Fig. 13).

485 There is an observable diagonal smearing of the resolved checkerboard patterns at the eastern
486 and western limits of the model, for all scales of velocity perturbation. This phenomenon
487 occurs between checks of equal polarity, at profile distances < 10 km and > 50 km. This
488 smearing is likely to be the result of the subsurface being sampled by unidirectional wave
489 propagation and limited data offsets in these areas of the model.

490 Large-scale structure (10.0 km x 2.0 km) is very well resolved throughout the central portion
491 of the model, but exhibits a small deterioration in the recovered anomaly amplitudes below
492 10 km depth. Medium-scale structure (5.0 km x 1.0 km) is still well resolved, but starts to
493 exhibit slight smearing between checks where there is lower instrument coverage (e.g. 5.0 –
494 30.0 km profile distance), and again at depths > 10 km. Fine-scale structure (2.5 km x 0.5
495 km) is the least well resolved, as is to be expected, but much of the structure at this scale is
496 still recoverable throughout the model. Fine-scale structure is particularly well resolved
497 between profile distances of 30.0 – 42.0 km and 52.0 – 60.0 km, where the coverage of
498 instruments is densest. Other regions of the model start to reveal a greater degree of smearing
499 between checks, primarily between diagonally linked checks.

500 The results of these resolution tests exhibit a significant improvement over the minimum
501 resolution of approximately 5.0 x 2.5 km, achieved in the travel-time tomography of Davy *et*
502 *al.* (2016). However, it should be noted that these resolution tests are done with synthetically
503 produced wavefields and thus represent the maximum achievable resolution with the given
504 experimental geometry.

505 **4 Results and discussion**

506 The final FWI velocity model in depth can be seen in Figs 4F and 6D. Overall, the long-
507 wavelength velocity structure remains consistent with that of the starting travel-time
508 tomography model. Within the velocity model we observe well-defined rotated continental
509 fault blocks which overlie the S-reflector, and the Peridotite Ridge in the west. The FWI
510 result reveals features in the velocity model with shorter-wavelengths and a greater lateral
511 variability to those that are observed in the starting model, indicating an increase in the
512 resolution of the velocity structure along this seismic line.

513 **4.1 Comparison with seismic images and interpretations**

514 In order to assess whether the FWI has resolved the velocities of fine-scale subsurface
515 structure, we compare the final velocity model with the structure observed in reflection
516 seismic imaging. To make this comparison we have utilised existing high-resolution 3D
517 multichannel reflection seismic images, which have been processed through to 3D pre-stack
518 Kirchhoff time migration. This reflection imaging was produced using the full 3D seismic
519 volume, which has a wide azimuth of shots and receivers, and yields a high-fidelity image of
520 the subsurface. We converted our final FWI velocity model to time, and overlaid it onto the
521 time migrated reflection image of seismic inline 420 (Figs 14 and 15). Additionally we have
522 overlain the interpretation of significant and relevant faults and geological horizons.
523 Significant horizon reflections are seen from the base of the post-rift sediment, a strong intra
524 syn-rift reflector, the top of crystalline basement, and the S-reflector. These interpretations
525 have been made consistently throughout the 3D seismic volume and are independent from
526 both our starting and FWI velocity models. For the prominent normal faults and continental
527 blocks observed through this section, we have adopted the naming convention of F3 – F8 and
528 B3 – B7, respectively (Ranero and Pérez-Gussinyé 2010; Borgmeyer 2010) .

529 **4.1.1 Long-wavelength structure**

530 Long-wavelength features that were already present in the starting velocity model show a
531 strong correlation with the large-scale features imaged in the reflection seismic, such as the
532 Peridotite Ridge, the major fault-rotated continental blocks (e.g. B3 – B6) and the S-reflector
533 detachment surface (Fig. 14D) (Davy *et al.* 2016). These features retain their long-
534 wavelength velocity structure through the FWI process, and shorter wavelength velocity
535 features are revealed within the previously resolved features. The most apparent and
536 significant changes to the velocity model occur in continental fault blocks B4-B7 within the
537 pre / syn-rift sediments and the top of crystalline basement. Areas of particular interest are
538 identified by dashed boxes in Fig. 14 and are shown at a larger scale in Fig. 15. Features
539 within these areas are discussed in detail in the next sub-section. Outside of these regions, we
540 observed noticeable features at both the western and eastern limits of the inversion model.

541 There is a deepening of seismic velocities between 6.0 – 7.0 km s⁻¹ on the eastern flank of the
542 Peridotite Ridge (7.0 – 12.0 km profile distance, arrow i, Fig. 14E). This deepening could
543 indicate that the serpentinisation of the mantle peridotite in this area is more pervasive than
544 previous models have indicated. This area of decreased seismic velocities is coincident with
545 the interpreted western limit of the S-reflector and the suggested location of normal fault F8,
546 which could have acted as a conduit, enabling the hydration and serpentinisation of this area.

547 At the eastern end of the profile, we observe top basement velocities (~ 5.5 km s⁻¹) resolved
548 in both blocks B3 and B2, east of their interpreted bounding faults, F4 and F3, respectively
549 (arrows ii and iii, Fig. 14E). The velocity in the up-dip end of the rotated fault blocks
550 increases to values consistent with crystalline basement, indicating that the internal structure
551 of these blocks is resolved to a greater degree. Additionally, there is a shallowing of mantle
552 velocities (~ 8.0 km s⁻¹) below continental block B2, which removes an apparent step in these
553 velocities observed in the starting model (arrow iv, Fig. 14E).

554

4.1.2 Continental fault blocks

555 The starting velocity model has minimal adherence to the interpreted geological horizons
556 within fault block B4 – B7 (Fig. 15D-F). Velocity contours cut across reflection horizons
557 obliquely, where they would be expected to run parallel, and no sharp velocity changes are
558 observed laterally across normal faults. Significant improvements are observed in the FWI
559 velocity model (arrows i-xiii in Fig. 15G-I), relative to the starting model, with an increased
560 correlation between the velocity field and a number of the interpreted faults and reflection
561 horizons. In some areas we also observe increased correlation between the velocity model
562 and seismic reflections, which have not been interpreted previously (dashed lines Fig.15G-I).
563 Particularly good improvement is observed in the internal velocity structure of continental
564 blocks B6 and B7 (arrows i-v, Fig. 15G-H, and to a lesser degree B6a and B5 (arrows vi-x,
565 Fig.15H). In these regions of the model we see a rotation of the velocity field, particularly at
566 the top of crystalline basement, so that velocity contours run parallel to significant
567 reflections. For example, in block B6 (Fig. 15E), starting velocities at the top of the
568 interpreted crystalline basement of $\sim 4.55 \text{ km s}^{-1}$ on the up dip (western) end, and $\sim 5.95 \text{ km}$
569 s^{-1} on the down dip end (eastern). This gives a velocity difference of $\sim 1.40 \text{ km s}^{-1}$ along a
570 lithological boundary where we would expect to observe a roughly constant velocity. After
571 the inversion the velocities in these same model locations are now $\sim 5.35 \text{ km s}^{-1}$ and ~ 5.65
572 km s^{-1} , up dip and down dip, respectively; a velocity difference of only $\sim 0.30 \text{ km s}^{-1}$ along
573 the same boundary. Similar improvements in the crystalline basement velocities are observed
574 in block B7 (Fig. 15D and G), and less substantial improvements are also seen in blocks B6a
575 and B5 (arrows vi and ix, Fig. 15E and H).

576 Despite not resolving constant velocities along the layer boundaries within block B4 (Fig.
577 15F and I), the FWI process has begun to introduce the appropriate higher velocities (~ 6.00
578 km s^{-1}) into the area interpreted as crystalline basement. These velocities are prominently

579 resolved next to the westward fault, F5 (arrow xii, Fig. 15I). The area of high velocity within
580 the crystalline basement of B4 now exhibits a large velocity contrast laterally across normal
581 fault F5, with the syn-rift unit of block B5 (arrow xi, Fig. 15I). We observe a lateral velocity
582 contrast of $\sim 1.70 \text{ km s}^{-1}$ over a distance of less than 1.00 km across fault F5, where the
583 starting contrast was previously $\sim 0.75 \text{ km s}^{-1}$. This result indicates an increased resolution of
584 the velocity changes across normal faults, which are inferred to have juxtaposed different
585 lithologies against one another. This improvement in the lateral velocity contrast is also
586 observed between the crystalline basement of block B6 and the syn-rift unit of block B7,
587 across fault F7 (arrow ii, Fig. 15G). There is also evidence of a previously unidentified fault
588 within block B6a, between faults F6 and F6a (Fig. 15H). A sharp lateral velocity contrast of
589 $\sim 1.50 \text{ km s}^{-1}$ (arrow viii, Fig. 15H), and westward dipping velocity field, highlights a weak
590 reflector which we interpret as a normal fault.

591 Even though these areas of the FWI model exhibit apparent improvement, there are areas
592 where we now observe velocity patterns which do not match the reflection image and its
593 interpretation. Within fault block B4 (Fig. 15I) a large portion of the unit interpreted as
594 crystalline basement remains unresolved, with uncharacteristically low velocities. There are
595 also areas where we observe a chaotic pattern in the velocities, exhibiting little correlation to
596 imaged sedimentary reflectors. A similar uncorrelated velocity pattern is observed in the
597 sedimentary units of block B5 (Fig. 15H-I). A small, and unlikely, circular velocity inversion
598 is observed directly east of fault F8 (Fig. 15G). These areas all appear to be well resolved in
599 the checkboard tests (Fig. 13), which suggests that these artefacts do not arise as a result of
600 the survey geometry. They may instead arise from the presence of out-of-plane arrivals
601 affecting the FWI, and cycle-skipping in the longer-offset data that is not corrected during
602 FWI (e.g. -14.92 km in Fig. 11C and I). While random noise within field data will be
603 attenuated through the FWI process, coherent noise, such as that from multiple energy, can be

604 mapped into false velocity structure (Pratt *et al.* 1998). It is difficult to determine where such
605 artefacts are to be expected, other than using qualitative model assessments, such as
606 comparisons with reflection imaging.

607 The final velocity model appears to have been resolved well in areas with seismic velocities
608 within the fault blocks of 2.80 – 5.20 km s⁻¹ for the syn- and pre-rift sediments, 5.20 –
609 6.50 km s⁻¹ for crystalline basement, and 6.50 – 8.50 km s⁻¹ for the uppermost mantle,
610 directly below the S-reflector. These typical unit velocities, and their associated boundary
611 velocities, enable us to reinterpret the reflection seismic image. Previous interpretations have
612 failed to identify continental fault block B7 (e.g. Borgmeyer 2010), or have interpreted it to
613 be a completely pre / syn-rift sedimentary unit, above the S-reflector (Fig. 15G). However,
614 seismic velocities indicative of crystalline basement (~ 6.00 km s⁻¹) allow us to reinterpret the
615 reflection horizons in this fault block. Where previous interpretations had indicated the
616 presence of the intra syn-rift reflector we now interpret this as the top of crystalline basement,
617 and the intra syn-rift reflector is reinterpreted above, along a reflector near the ~ 4.90 km s⁻¹
618 velocity contour. We have also reinterpreted the intra syn-rift reflector in fault block B6
619 (Fig. 15H). Velocities in this unit do not support the reflector pinching out to the west, as
620 originally suggested, but instead suggest that it maintains a consistent thickness, following a
621 consistent velocity of ~ 4.90 km s⁻¹ and matches a prominent reflector in the seismic image.
622 Additionally, the intra syn-rift reflector is reinterpreted between fault F6a and the newly
623 interpreted fault (Fig. 15H).

624 The interpretation of the smallest continental fault block, B7, agrees with the sequential
625 faulting model, which predicts that the continental blocks decrease in size oceanward.
626 However, the interpretation of previously unidentified normal faulting, combined with the
627 observation of irregular basement and syn-rift velocities, within previously identified fault
628 blocks (see Fig. 15H) indicates that the pattern of deformation within the hyperextended

629 domain is more complicated than that described by the sequential faulting model. These
630 interpretations could suggest that there was an earlier phase of faulting, which has
631 subsequently been overprinted by the large dominant normal faults which are observed in the
632 reflection seismic images. Such interpretations would give favour to polyphase faulting
633 models, which describe complex fault overprinting, and contradict the sequential faulting
634 model.

635 **4.2 S-reflector and associated velocities**

636 The S-reflector represents a significant velocity contrast between rocks of the lower-crust
637 juxtaposed against upper-mantle peridotites which have been serpentinised to varying
638 degrees. Our starting model exhibits a relatively low velocity contrast across the S-reflector,
639 which is the result of the smooth nature of the travel-time tomography modelling. However,
640 we see a sharpening of the velocity contrast over the S-reflector in the FWI model, indicating
641 that the velocities directly above and below the fault surface are being resolved to a greater
642 degree. This is particularly well observed below fault blocks B4, B5 and B6a, where the
643 average velocity contrasts (difference between velocities 50 ms above and below the mapped
644 S-reflector surface) increase from 0.25, 0.39, and 0.39 km s^{-1} , to 0.50, 0.68, and 0.55 km s^{-1} ,
645 respectively. In reality, the velocity contrast across the S-reflector is likely to be sharper than
646 that observed in Figures 14E and 15G-H, however, the resolution of the FWI is limited by the
647 relatively low inversion frequencies used (3.0 – 5.2 Hz).

648 It is difficult to gauge from the 2D velocity plots whether there has been an improvement in
649 the velocities associated with serpentinisation of upper mantle peridotite along and below the
650 S-reflector. The interaction between normal faulting and the P-wave velocities below the
651 S-reflector is more apparent plotted as velocity against distance. Velocities averaged over a
652 100 ms window below the mapped S-reflector are plotted against the profile distance, for

653 both the starting and inversion velocity model (Fig. 16). The starting model exhibits a general
654 pattern of preferential mantle serpentinisation, which is observed as relative decreases in the
655 seismic velocity down-dip of normal faults (Davy *et al.* 2016). This trend is particularly
656 evident down-dip of faults F6 and F7. However, in this model slight increases in the velocity
657 down-dip of faults F5 and F6a can be observed, before the expected velocity decrease. These
658 velocity increases, despite being minor, contradict the hypothesis of preferential hydration
659 and serpentinisation of the mantle by normal faulting.

660 In the same figure it can be seen that the FWI result has resolved the pattern of preferential
661 mantle serpentinisation in greater detail. Decreases in seismic velocity are now seen directly
662 down-dip of normal faults, F5 – F8 (Fig. 16). This result is more consistent than the starting
663 model with the hypothesis that normal faults act as conduits, enabling the preferential
664 hydration and serpentinisation of upper mantle peridotites below the S-reflector (Bayrakci *et*
665 *al.* 2016; Davy *et al.* 2016). We interpret the consistently low velocities between faults F4
666 and F5 to be indicative of crustal material, and interpret the S-reflector as being intra-crustal
667 in this region of the model. Despite this promising result, there are unexpected features in the
668 velocity profile of the FWI model.

669 We observe two short-wavelength (~ 2 km) feature which show anomalously rapid change in
670 seismic velocity (highlighted by red dashed ellipsoid in Fig. 16). The most prominent exhibits
671 an increase in velocity of ~ 1.5 km s⁻¹ at 41 km profile distance. This rapid change appears to
672 be particularly anomalous, when compared with the rest of the profile, and differs greatly
673 from the velocity trend in both the starting and inversion models. The other anomalous
674 feature is coincident with fault F5, and reaches the model's maximum allowed velocity of
675 8.50 km s⁻¹. We expect the velocity of unaltered upper mantle peridotite to be ~ 8.00 km s⁻¹,
676 thus making this observation implausible (e.g., Carlson and Miller 2003). These features
677 appear to be artefacts introduced during the FWI process. It is possible that these features

678 arise due to the sparsity of data available in this experiment, or are the result of the FWI
679 process trying to map coherent noise into the velocity model.

680 Unfortunately, in order to resolve the velocity structure at these depths, we had to include
681 data that were starting to be affected by coherent multiple noise from the previous seismic
682 shot. Increasing the time between shots would enable greater depth resolution, at the expense
683 of degrading the 3D reflection image that was the primary aim of the experiment. Ignoring
684 these anomalous short-wavelength features, we can attempt to quantify the levels of observed
685 serpentinisation. Relative velocity decreases (from the normal fault to the nearest down-dip
686 velocity minima) of $\sim 0.60 \text{ km s}^{-1}$, $\sim 0.60 \text{ km s}^{-1}$, $\sim 0.70 \text{ km s}^{-1}$ and $\sim 1.0 \text{ km s}^{-1}$ are observed
687 for faults F5, F6a, F6 and F7, respectively. Using the study of Carlson and Miller (2003) we
688 can approximate the extent of mantle peridotite serpentinisation, based on the observed P-
689 wave velocities. Down-dip of these faults we calculate the degree of serpentinisation,
690 averaged over the resolution length of the FWI, to change from 0 to 20%, 30 to 40%, 30 to
691 50% and 30 to 60%, for faults F5, F6a, F6 and F7, respectively.

692

693 **5 Conclusions**

694 The application of FWI has yielded a clear improvement over travel-time tomography results.

695 From this study we find that:

- 696 • FWI can be applied to sparse and noisy OBS data in deep water environments, for the
697 purpose of producing high-resolution velocity models of shallow (< 10 km below
698 seafloor) crustal targets.
- 699 • The final FWI result is limited by the sparsity of data available, and the presence of
700 coherent noise at longer data offsets.

- 701 • The final velocity model exhibits a significant increase in resolution within the
702 continental fault blocks of this hyperextended domain. This improvement in the
703 velocity model has enabled the reinterpretation of the reflection seismic image
- 704 • Newly interpreted faults, within the existing continental blocks, may provide evidence
705 for an earlier phase of faulting which has subsequently been overprinted by the block
706 bounding normal faults. Such an interpretation would lend support to polyphase
707 models of faulting within the hyperextended domain.
- 708 • Increased resolution in the seismic velocities below the S-reflector has further defined
709 the pattern of upper mantle serpentinisation, a result of preferential hydration by
710 normal faults acting as water conduits. The degree of preferential mantle
711 serpentinisation is interpreted to vary between 20 – 60%.

712 Given a more optimised seismic shooting period we can expect that the results would have
713 shown an even greater quality. Increasing the time between subsequent seismic shots would
714 allow time for energy of the previous shot to dissipate, reducing the coherent noise in the
715 recorded data and enabling greater depth resolution of the FWI method. We suggest that
716 future marine studies, targeting crustal structure, take into consideration the application of
717 FWI to their proposed datasets. While a higher density of OBS/H is desirable, we have shown
718 that a relatively sparse profile can improve the resolution of travel-time tomography models.
719 This approach will also allow for the improved migration of reflection seismic images, which
720 was not investigated here. There may also be merit in applying the FWI method to existing
721 high quality 2D OBS/H datasets where high quality travel-time tomography models have
722 already been determined.

723 **6 Acknowledgements**

724 We thank the sponsors of the FULLWAVE consortia for support in developing the FWI
725 software used here. Data acquisition was supported by the US National Science Foundation,
726 the UK Natural Environment Research Council (grant NE/E016502/1) and GEOMAR
727 Helmholtz Centre for Ocean Research. T.A.M. was supported by a Wolfson Research Merit
728 award. Ocean bottom instrumentation was provided by the UK Ocean Bottom
729 Instrumentation Facility and by GEOMAR Helmholtz Centre for Ocean Research. We would
730 like to thank everyone who participated and contributed hard work to the data acquisition,
731 either aboard the R/V Marcus Langseth or the F/S Poseidon. Additionally we would like to
732 thank the two reviewers, Gail Christenson and Emilie Hooft, who provided excellent
733 feedback which has greatly helped refine the manuscript. The wide angle seismic data used in
734 this study can be accessed at <https://doi.pangaea.de/10.1594/PANGAEA.859069>.

735 **References**

- 736 Arnoux, G.M., Toomey, D.R., Hooft, E.E., Wilcock, W.S., Morgan, J., Warner, M. & VanderBeek, B.P.,
737 2017. Seismic evidence that black smoker heat flux is influenced by localized magma
738 replenishment and associated increases in crustal permeability, *Geophysical Research*
739 *Letters*, 44, 1687-1695.
- 740 Bayrakci, G., Minshull, T., Sawyer, D., Reston, T.J., Klaeschen, D., Papenberg, C., Ranero, C., Bull, J.,
741 Davy, R. & Shillington, D., 2016. Fault-controlled hydration of the upper mantle during
742 continental rifting, *Nature Geoscience*, 9, 384-388.
- 743 Beslier, M.-O., Ask, M. & Boillot, G., 1993. Ocean-continent boundary in the Iberia Abyssal Plain from
744 multichannel seismic data, *Tectonophysics*, 218, 383-393.
- 745 Boillot, G., Winterer, E. & Meyer, A., 1987. Introduction, objectives, and principal results: Ocean
746 Drilling Program Leg 103, west Galicia Margin, *Proc. Ocean Drill. Program, Initial Reports*,
747 103, 3-17.
- 748 Borgmeyer, A.L., 2010. Three-dimensional geometries of rifting on a hyperextended margin-
749 Interpretation of seismic reflection profiles from the Deep Galicia Basin, Iberia, MSc thesis
750 MSc, Rice University.
- 751 Brossier, R., Operto, S. & Virieux, J., 2009. Seismic imaging of complex onshore structures by 2D
752 elastic frequency-domain full-waveform inversion, *Geophysics*, 74, WCC105-WCC118.
- 753 Bunks, C., Saleck, F.M., Zaleski, S. & Chavent, G., 1995. Multiscale seismic waveform inversion,
754 *Geophysics*, 60, 1457-1473.
- 755 Carlson, R.L. & Miller, D.J., 2003. Mantle wedge water contents estimated from seismic velocities in
756 partially serpentinized peridotites, *Geophysical Research Letters*, 30, 1250.
- 757 Davy, R., Minshull, T., Bayrakci, G., Bull, J., Klaeschen, D., Papenberg, C., Reston, T.J., Sawyer, D. &
758 Zelt, C., 2016. Continental hyperextension, mantle exhumation, and thin oceanic crust at the
759 continent-ocean transition, West Iberia: New insights from wide-angle seismic, *Journal of*
760 *Geophysical Research: Solid Earth*, 121, 3177-3199.

761 Dean, S., Sawyer, D. & Morgan, J., 2015. Galicia Bank ocean–continent transition zone: New seismic
762 reflection constraints, *Earth and Planetary Science Letters*, 413, 197-207.

763 Dessa, J.X., Operto, S., Kodaira, S., Nakanishi, A., Pascal, G., Virieux, J. & Kaneda, Y., 2004. Multiscale
764 seismic imaging of the eastern Nankai trough by full waveform inversion, *Geophysical
765 Research Letters*, 31, L18606.

766 Gardner, G., Gardner, L. & Gregory, A., 1974. Formation velocity and density—The diagnostic basics
767 for stratigraphic traps, *Geophysics*, 39, 770-780.

768 Jaiswal, P., Zelt, C.A., Bally, A.W. & Dasgupta, R., 2008. 2-D traveltimes and waveform inversion for
769 improved seismic imaging: Naga Thrust and Fold Belt, India, *Geophysical Journal
770 International*, 173, 642-658.

771 Jones, C., Evans, M., Ratcliffe, A., Conroy, G., Jupp, R., Selvage, J. & Ramsey, L., 2013. Full waveform
772 inversion in a complex geological setting—a narrow azimuth towed streamer case study from
773 the Barents Sea. in *Proceedings of the 75th EAGE Conference*, Extended Abstracts.

774 Kamei, R., Pratt, R.G. & Tsuji, T., 2012. Waveform tomography imaging of a megasplay fault system
775 in the seismogenic Nankai subduction zone, *Earth and Planetary Science Letters*, 317, 343-
776 353.

777 Kapoor, S., Vigh, D., Wiarda, E. & Alwon, S., 2013. Full waveform inversion around the world. in
778 *Proceedings of the 75th EAGE Conference*, Extended Abstracts, doi: 10.3997/2214-
779 4609.20130827.

780 Kolb, P., Collino, F. & Lailly, P., 1986. Pre-stack inversion of a 1-D medium, *Proceedings of the IEEE*,
781 74, 498-508.

782 Korenaga, J., Holbrook, W., Kent, G., Kelemen, P., Detrick, R., Larsen, H.C., Hopper, J. & Dahl-Jensen,
783 T., 2000. Crustal structure of the southeast Greenland margin from joint refraction and
784 reflection seismic tomography, *Journal of Geophysical Research: Solid Earth*, 105, 21591-
785 21614.

786 Lailly, P., 1983. The seismic inverse problem as a sequence of before stack migrations. in *Conference
787 on Inverse Scattering: Theory and Application*, ed J. Bee Bednar, R. R., Enders Robinson. Soc.
788 Industr. Appl. Math., Philadelphia.

789 McDermott, K. & Reston, T., 2015. To see, or not to see? Rifted margin extension, *Geology*, 43, 967-
790 970.

791 Minshull, T.A., Sinha, M.C. & Peirce, C., 2005. Multi-disciplinary, sub-seabed geophysical imaging,
792 *Sea Technology*, 46, 27-31.

793 Mispel, J., Houbiers, M., Knudsen, B. & Amundsen, L., 2013. FWI with OBC Data From the Mariner
794 Field, UK-The Impact on Mapping Sands at Reservoir Level. in *Proceedings of the 75th EAGE
795 Conference*, Extended Abstracts, doi: 10.3997/2214-4609.20130829.

796 Morgan, J., Warner, M., Arnoux, G., Hooft, E., Toomey, D., VanderBeek, B. & Wilcock, W., 2016.
797 Next-generation seismic experiments—II: wide-angle, multi-azimuth, 3-D, full-waveform
798 inversion of sparse field data, *Geophysical Journal International*, 204, 1342-1363.

799 Morgan, J., Warner, M., Bell, R., Ashley, J., Barnes, D., Little, R., Roele, K. & Jones, C., 2013. Next-
800 generation seismic experiments: wide-angle, multi-azimuth, three-dimensional, full-
801 waveform inversion, *Geophysical Journal International*, 195, 1657-1678.

802 Mothi, S., Schwarz, K. & Zhu, H., 2013. Impact of full-azimuth and long-offset acquisition on Full
803 Waveform Inversion in deep water Gulf of Mexico. in *Proceedings of the 75th EAGE
804 Conference*, Extended Abstracts, doi: 10.1190/segam2013-0102.1.

805 Operto, S., Virieux, J., Amestoy, P., L'Excellent, J.-Y., Giraud, L. & Ali, H.B.H., 2007. 3D finite-
806 difference frequency-domain modeling of visco-acoustic wave propagation using a massively
807 parallel direct solver: A feasibility study, *Geophysics*, 72, SM195-SM211.

808 Operto, S., Virieux, J., Dessa, J.X. & Pascal, G., 2006. Crustal seismic imaging from multifold ocean
809 bottom seismometer data by frequency domain full waveform tomography: Application to
810 the eastern Nankai trough, *Journal of Geophysical Research: Solid Earth*, 111, B09306.

811 Pérez-Gussinyé, M., 2013. A tectonic model for hyperextension at magma-poor rifted margins: an
812 example from the West Iberia–Newfoundland conjugate margins, *Geological Society,*
813 *London, Special Publications*, 369, 403-427.

814 Pérez-Gussinyé, M., Ranero, C., Reston, T.J. & Sawyer, D., 2003. Mechanisms of extension at
815 nonvolcanic margins: Evidence from the Galicia interior basin, west of Iberia, *Journal of*
816 *Geophysical Research: Solid Earth*, 108, 2245.

817 Pérez-Gussinyé, M. & Reston, T.J., 2001. Rheological evolution during extension at nonvolcanic rifted
818 margins: onset of serpentinization and development of detachments leading to continental
819 breakup, *Journal of Geophysical Research: Solid Earth*, 106, 3961-3975.

820 Pratt, R.G., 1999. Seismic waveform inversion in the frequency domain, Part 1: Theory and
821 verification in a physical scale model, *Geophysics*, 64, 888-901.

822 Pratt, R.G., Shin, C. & Hick, G., 1998. Gauss–Newton and full Newton methods in frequency–space
823 seismic waveform inversion, *Geophysical Journal International*, 133, 341-362.

824 Ranero, C.R. & Pérez-Gussinyé, M., 2010. Sequential faulting explains the asymmetry and extension
825 discrepancy of conjugate margins, *Nature*, 468, 294-299.

826 Ratcliffe, A., Win, C., Vinje, V., Conroy, G., Warner, M., Umpleby, A., Stekl, I., Nangoo, T. & Bertrand,
827 A., 2011. Full waveform inversion: A North Sea OBC case study. *in 2011 SEG Annual Meeting,*
828 *Society of Exploration Geophysicists, Expanded Abstracts* 30, pp. 2384–2388.

829 Reston, T. & McDermott, K., 2014. An assessment of the cause of the ‘extension discrepancy’ with
830 reference to the west Galicia margin, *Basin Research*, 26, 135-153.

831 Reston, T.J., 2009. The structure, evolution and symmetry of the magma-poor rifted margins of the
832 North and Central Atlantic: a synthesis, *Tectonophysics*, 468, 6-27.

833 Reston, T.J., Leythäuser, T., Booth-Rea, G., Sawyer, D., Klaeschen, D. & Long, C., 2007. Movement
834 along a low-angle normal fault: The S reflector west of Spain, *Geochemistry, Geophysics,*
835 *Geosystems*, 8, Q06002.

836 Sawyer, D.S., Reston, T., Gussinye, M.P., Zelt, C.A., Austin, J.A., Nakamura, Y., Danobeitia, J. &
837 Cordoba, D., 1997. The Iberia Seismic Experiment (ISE97): MCS reflection profiles, *EOS*, 78.

838 Sirgue, L., 2006. The importance of low frequency and large offset in waveform inversion. *in*
839 *Proceedings of the 68th EAGE Conference*, Extended Abstracts, doi: 10.3997/2214-
840 4609.201402146.

841 Sirgue, L., Barkved, O., Dellinger, J., Etgen, J., Albertin, U. & Kommedal, J., 2010. Thematic set: Full
842 waveform inversion: The next leap forward in imaging at Valhall, *First Break*, 28, 65-70.

843 Srivastava, S., Sibuet, J.-C., Cande, S., Roest, W. & Reid, I.D., 2000. Magnetic evidence for slow
844 seafloor spreading during the formation of the Newfoundland and Iberian margins, *Earth*
845 *and Planetary Science Letters*, 182, 61-76.

846 Tarantola, A., 1984. Inversion of seismic reflection data in the acoustic approximation, *Geophysics*,
847 49, 1259-1266.

848 Tarantola, A., 1987. *Inverse Problem Theory: Models for Data Fitting and Model Parameter*
849 *Estimation* Elsevier, Amsterdam.

850 Virieux, J., 1986. P-SV wave propagation in heterogeneous media: Velocity-stress finite-difference
851 method, *Geophysics*, 51, 889-901.

852 Virieux, J. & Operto, S., 2009. An overview of full-waveform inversion in exploration geophysics,
853 *Geophysics*, 74, WCC1-WCC26.

854 Warner, M., Ratcliffe, A., Nangoo, T., Morgan, J., Umpleby, A., Shah, N., Vinje, V., Štekl, I., Guasch, L.
855 & Win, C., 2013. Anisotropic 3D full-waveform inversion, *Geophysics*, 78, R59-R80.

856 Warner, M., Umpleby, A., Stekl, I. & Morgan, J., 2010. 3D full-wavefield tomography: imaging
857 beneath heterogeneous overburden. *in Proceedings of the 72nd EAGE Conference*, Extended
858 Abstracts, doi: 10.3997/2214-4609.20149944

859 Williamson, P., 1991. A guide to the limits of resolution imposed by scattering in ray tomography,
860 *Geophysics*, 56, 202-207.

861 Wu, R.-S. & Töksöz, M.N., 1987. Diffraction tomography and multisource holography applied to
862 seismic imaging, *Geophysics*, 52, 11-25.
863 Zelt, C.A. & Barton, P.J., 1998. Three-dimensional seismic refraction tomography: A comparison of
864 two methods applied to data from the Faeroe Basin, *Journal of Geophysical Research: Solid
865 Earth*, 103, 7187-7210.
866 Zelt, C.A., Sain, K., Naumenko, J.V. & Sawyer, D.S., 2003. Assessment of crustal velocity models using
867 seismic refraction and reflection tomography, *Geophysical Journal International*, 153, 609-
868 626.

869

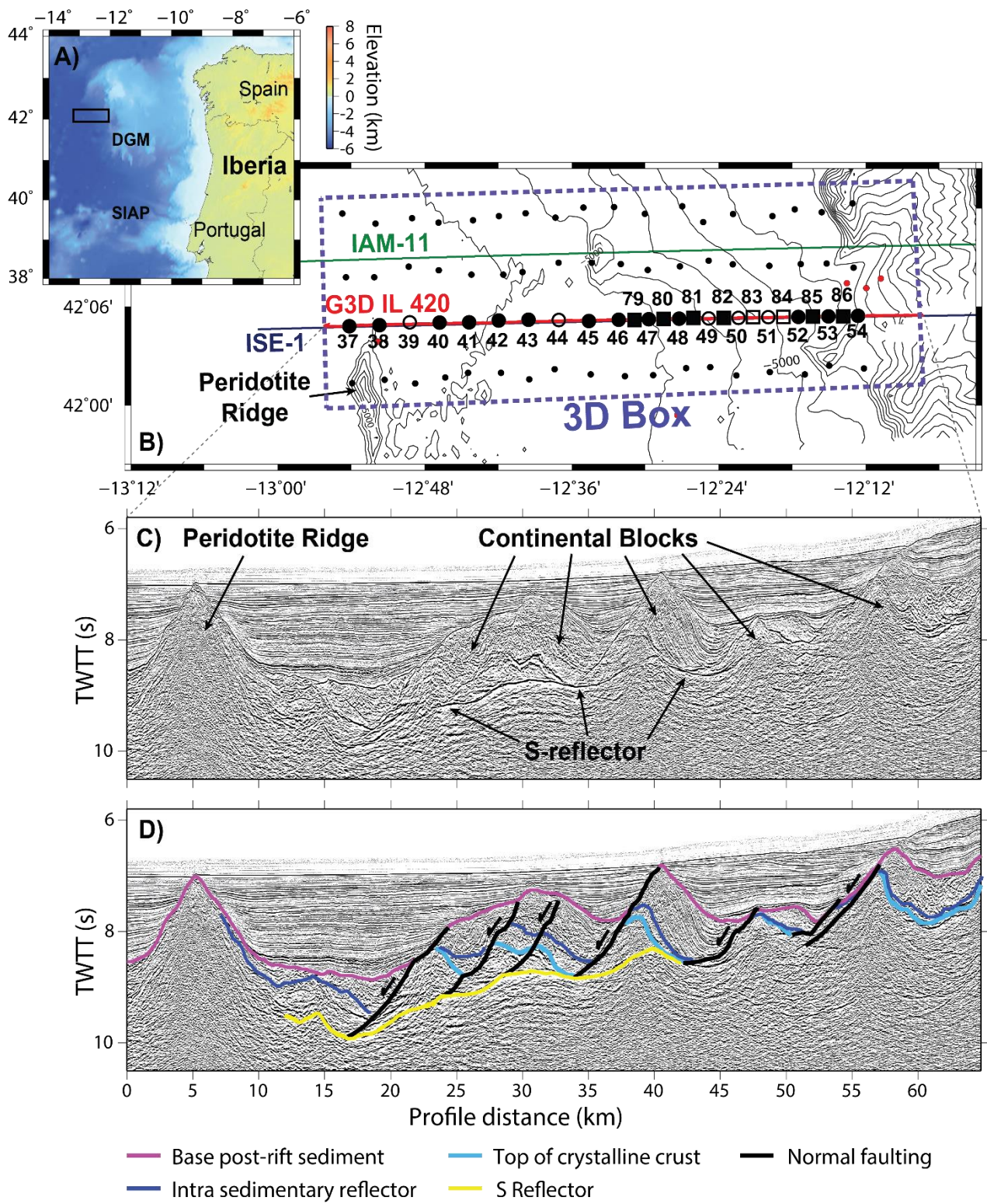
870 **Tables**

Inversion low-pass frequency	Reduction in misfit functional
3.0 Hz	9.2%
3.4 Hz	2.2%
3.9 Hz	2.4%
4.5 Hz	1.8%
5.2 Hz	2.5%

871 Table 1: Reduction in misfit functional for given inversion low-pass frequencies. Each
872 frequency is iterated 10 times.

873 **Figures**

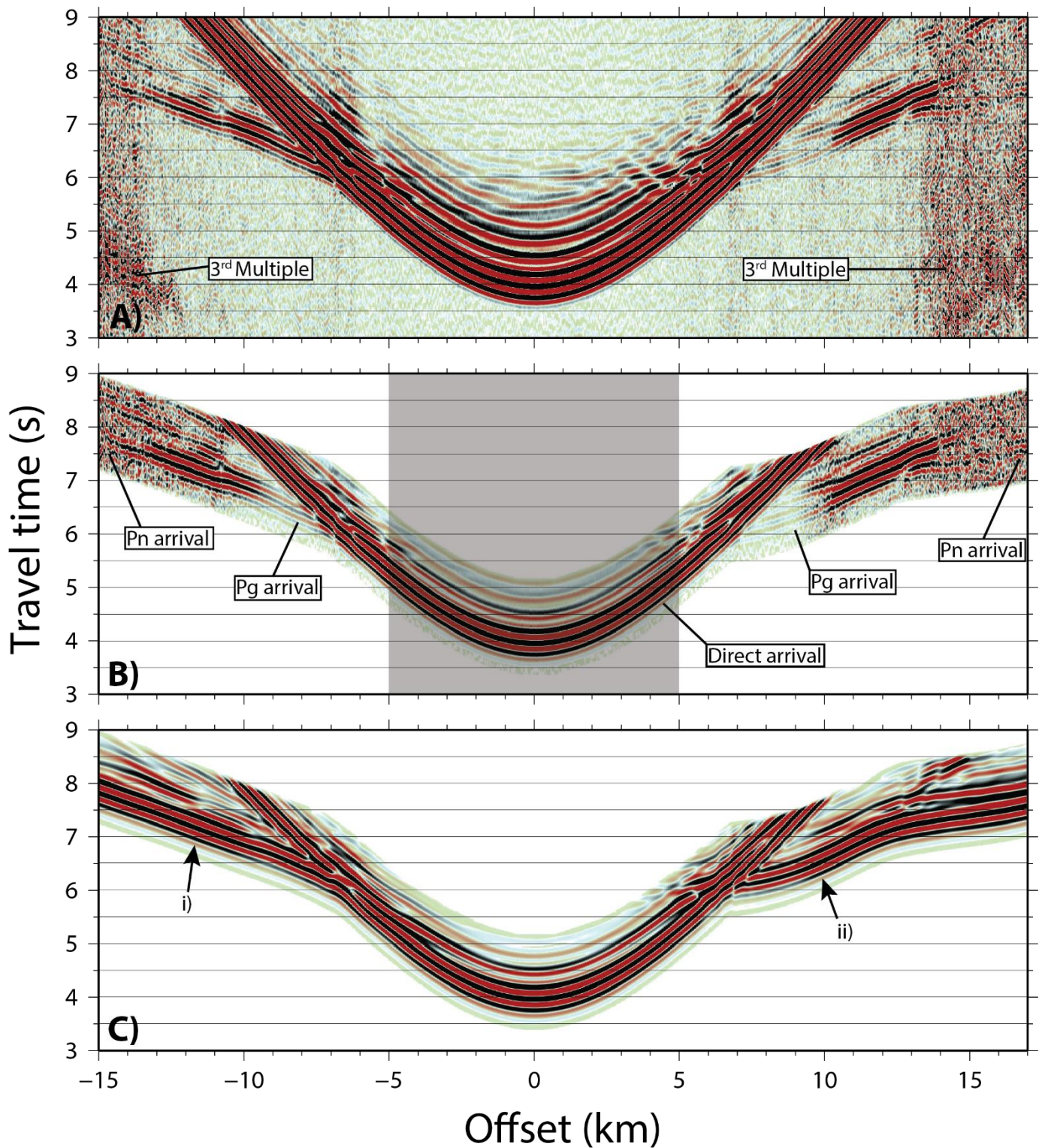
874 Start on next page. Note – I have made figures as big as possible for review. Sizes to be
875 adjusted for publication.



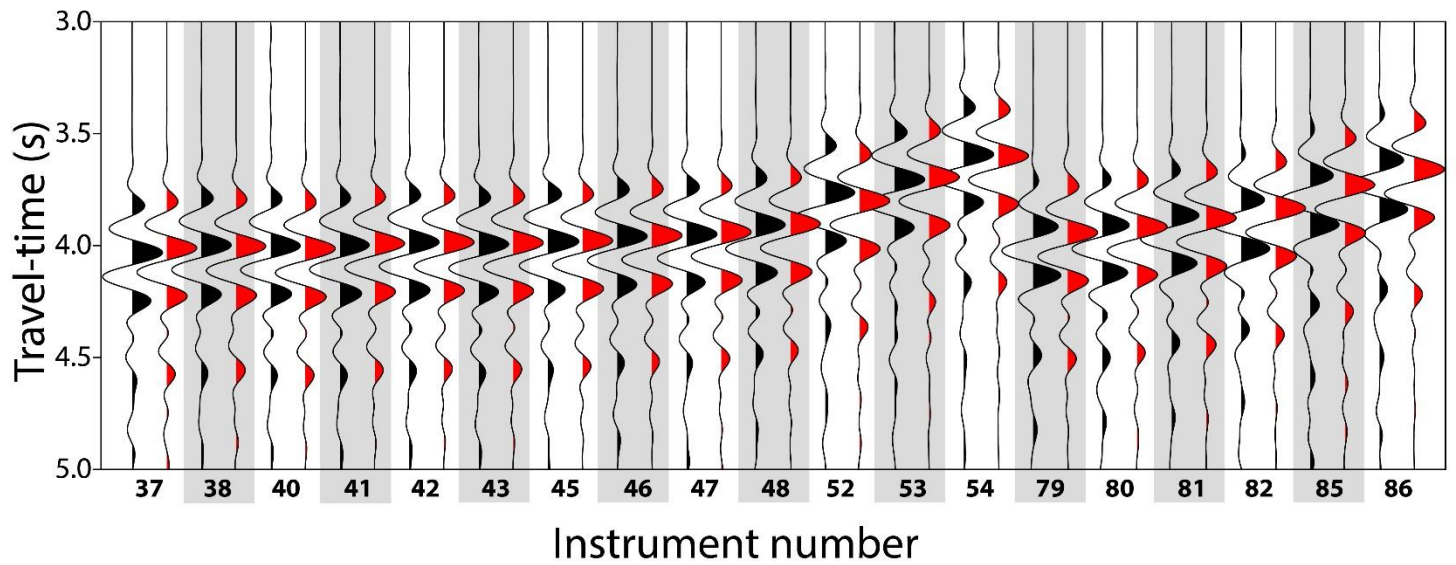
876

877 Figure 1: A) Bathymetric map of the Deep Galicia Margin (DGM) and the Southern Iberia
 878 Abyssal Plain (SIAP) with the relative location of Fig. 1B (black rectangle). B) Map of the
 879 Galicia-3D seismic experiment. Galicia 3-D inline 420 seismic profile is illustrated by a red

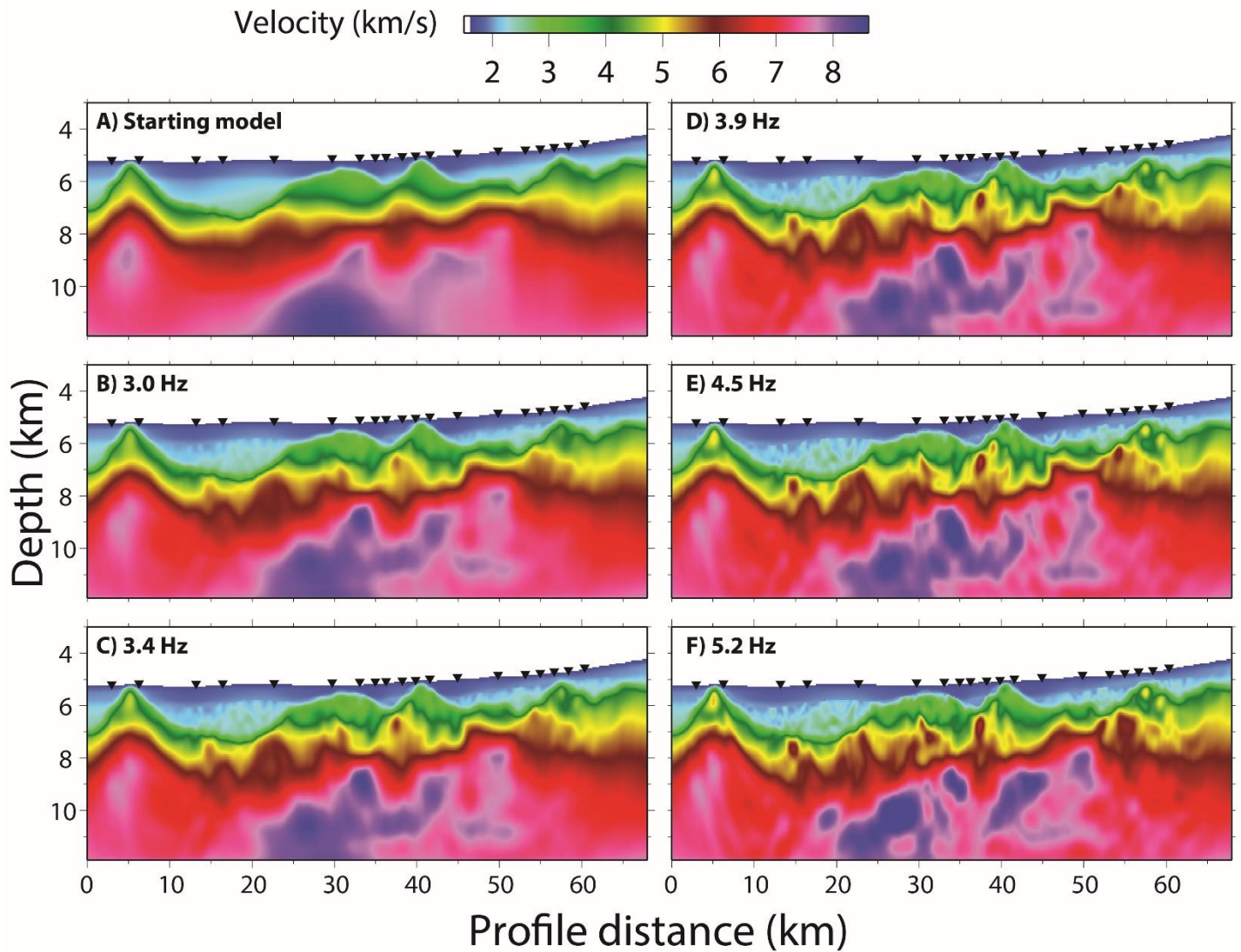
880 line; large black circles indicate the location of OBIF OBS along seismic inline 420; large
881 black squares indicate GEOMAR OBH; unfilled circles and squares indicate instruments
882 which recovered no data or were excluded from the FWI process. Purple line indicates the
883 ISE-1 seismic profile; green line indicates the IAM-11 seismic profile; ODP Leg 103 sites are
884 indicated by red circles (Boillot *et al.* 1987). C) Kirchhoff pre-stack time-migrated
885 multichannel seismic reflection image of inline 420, highlighting features of the Deep Galicia
886 Margin. D) Simplified interpretation of C).



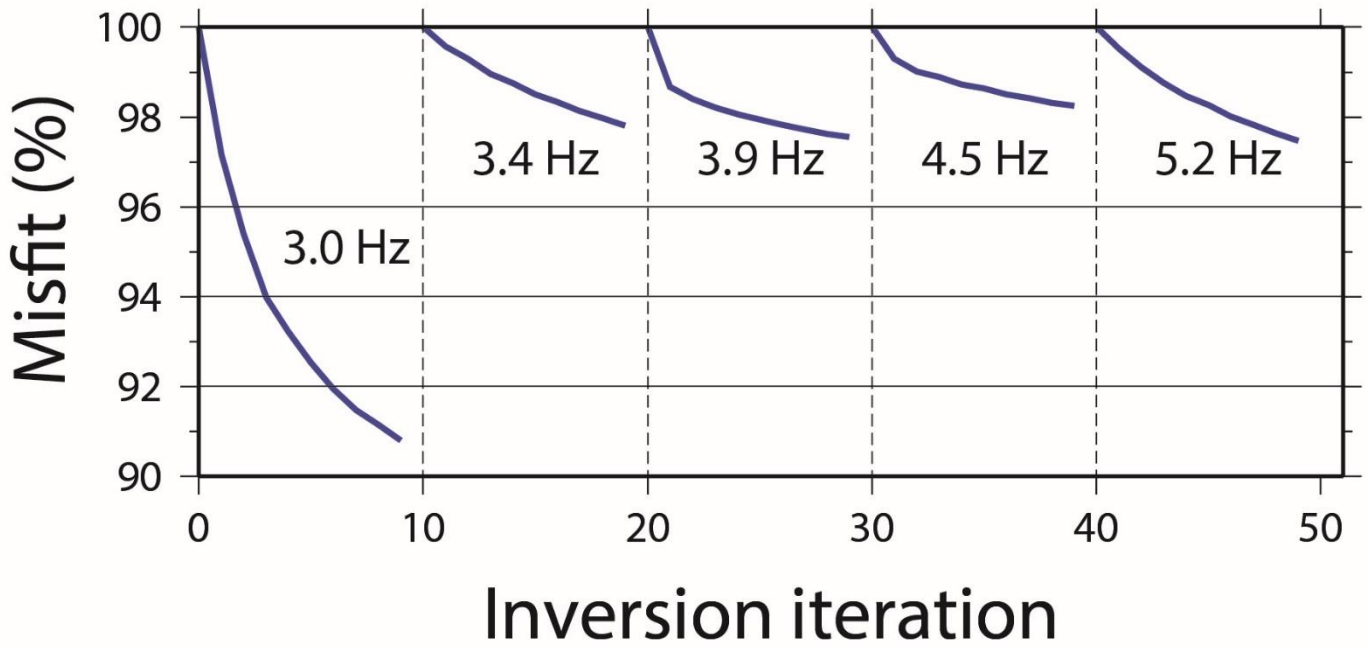
887 Figure 2: A) Example receiver gather from OBS 46, filtered with an Ormsby band-pass
 888 comprised of corner frequencies 2-3-4.5-6.5 Hz. The 3rd multiple from the previous seismic
 889 shot is indicated. B) Same receiver gather as in A), windowed 1.8 s after the first arrival for
 890 input into the inversion process. Grey area indicates data excluded from the inversion.
 891 Identified seismic phases are indicated. C) Synthetic receiver gather for OBS46 generated
 892 using the starting velocity model in Fig 4A.



893 Figure 3: Fit between observed and synthetic direct water wave arrivals. Observed near-offset
 894 traces (black) compared with the equivalent synthetic trace (red) through the starting velocity
 895 model, for all instruments used in this study. Observed data are band-pass filtered (Ormsby,
 896 corner frequencies 2-3-4.5-6.5 Hz).



897 Figure 4: A) Starting velocity model input to the FWI. Results of the iterative FWI process
 898 for low-pass filter frequencies of: B) 3.0 Hz; C) 3.4 Hz; D) 3.9 Hz; E) 4.5 Hz and F) 5.2 Hz.
 899 Black upturned triangles indicate the locations of utilised instruments. Vertical exaggeration
 900 is 3.2.



901 Figure 5: Misfit reduction versus inversion iterations for the five low-cut frequency bands,
 902 3.0, 3.4, 3.9, 4.5 and 5.2 Hz.

903

904

905

906

907

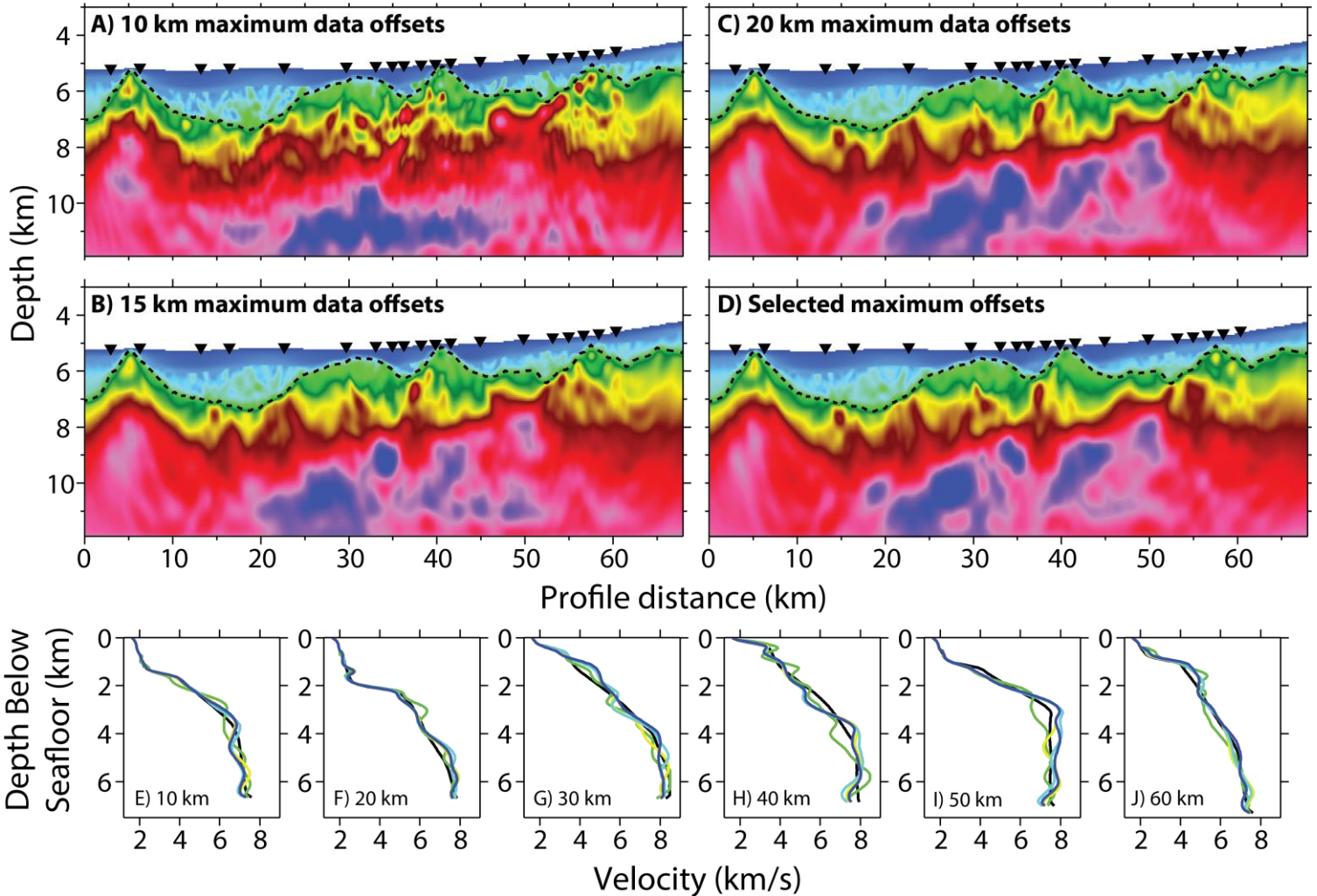
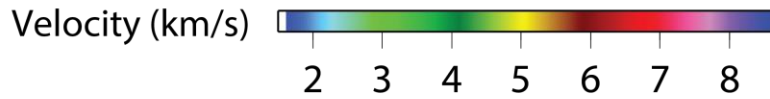
908

909

910

911

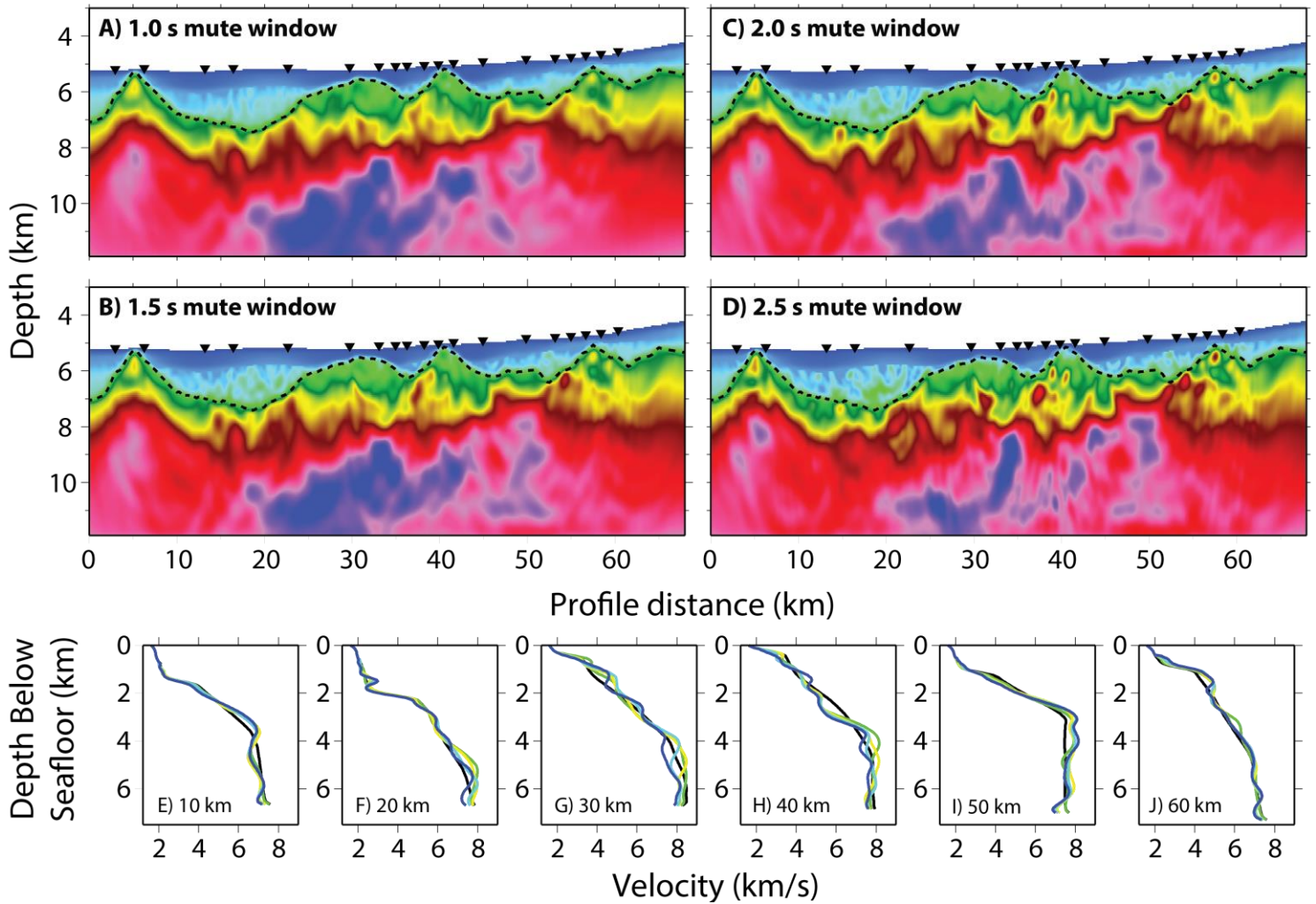
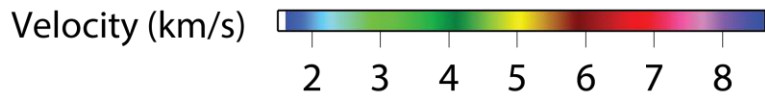
912



913 Figure 6: Inversion models for maximum data offsets of A) 10 km B) 15 km C) 20 km D)
 914 Instrument specific offsets. Black upturned triangles indicate the locations of utilised
 915 instruments, black dashed line indicates the base of post-rift sediments. Vertical exaggeration
 916 is 3.2. E-J) 1D velocity profiles through the resulting models, below the seafloor, at set
 917 profile distances (10, 20, 30, 40, 50 and 60 km, respectively). Line colours are black: starting
 918 model, green: 10 km data offsets, yellow: 15 km data offsets, light blue: 20 km data offsets,
 919 blue: instrument specific data offsets.

920

921



922

923 Figure 7: Inversion models for varying mute windows of A) 1.0 s B) 1.5 s C) 2.0 s D) 2.5 s.

924 Black upturned triangles indicate the locations of utilised instruments, black dashed line

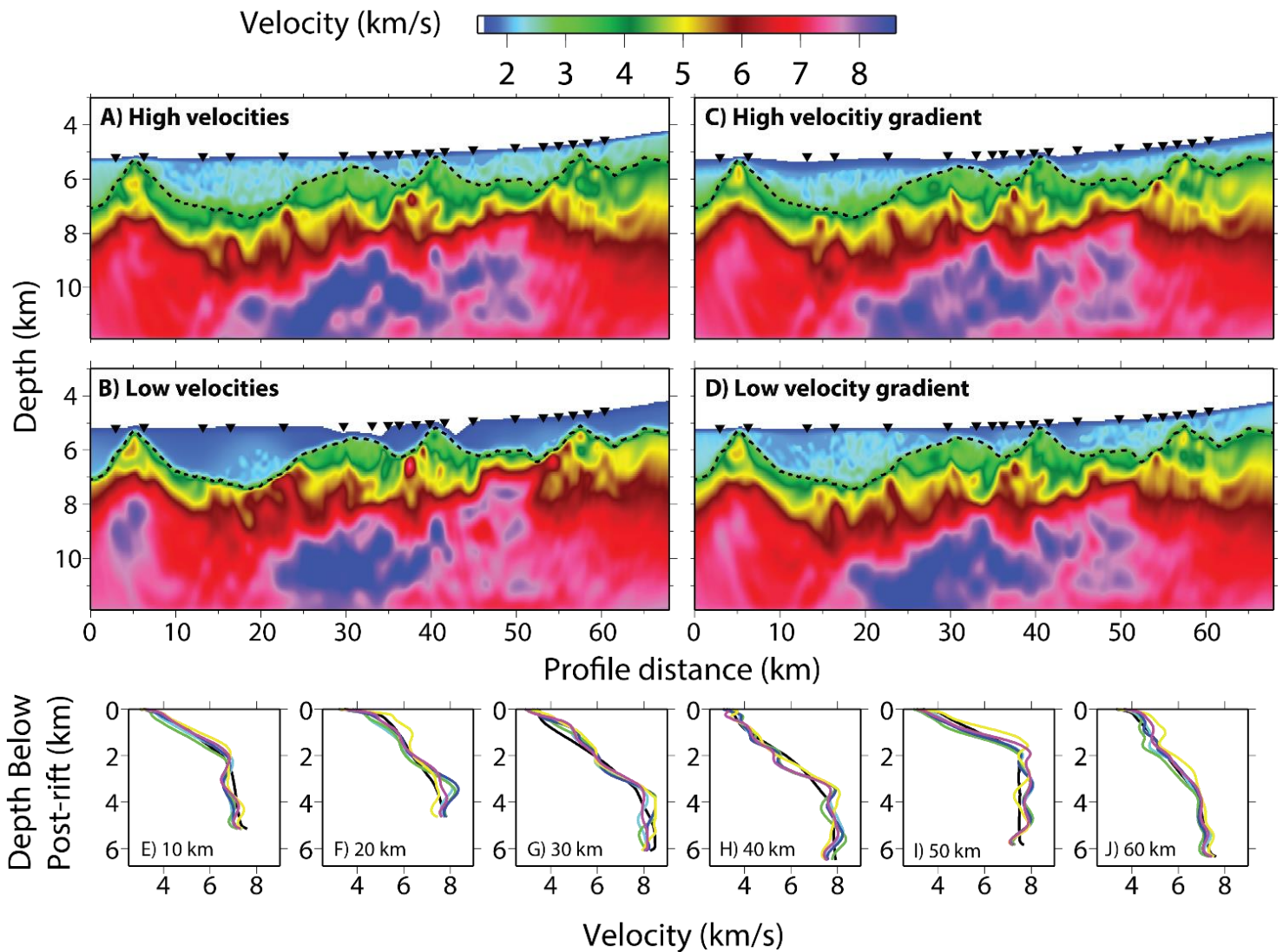
925 indicates the base of post-rift sediments. Vertical exaggeration is 3.2. E-J) 1D velocity

926 profiles through the resulting models, below the seafloor, at set profile distances (10, 20, 30,

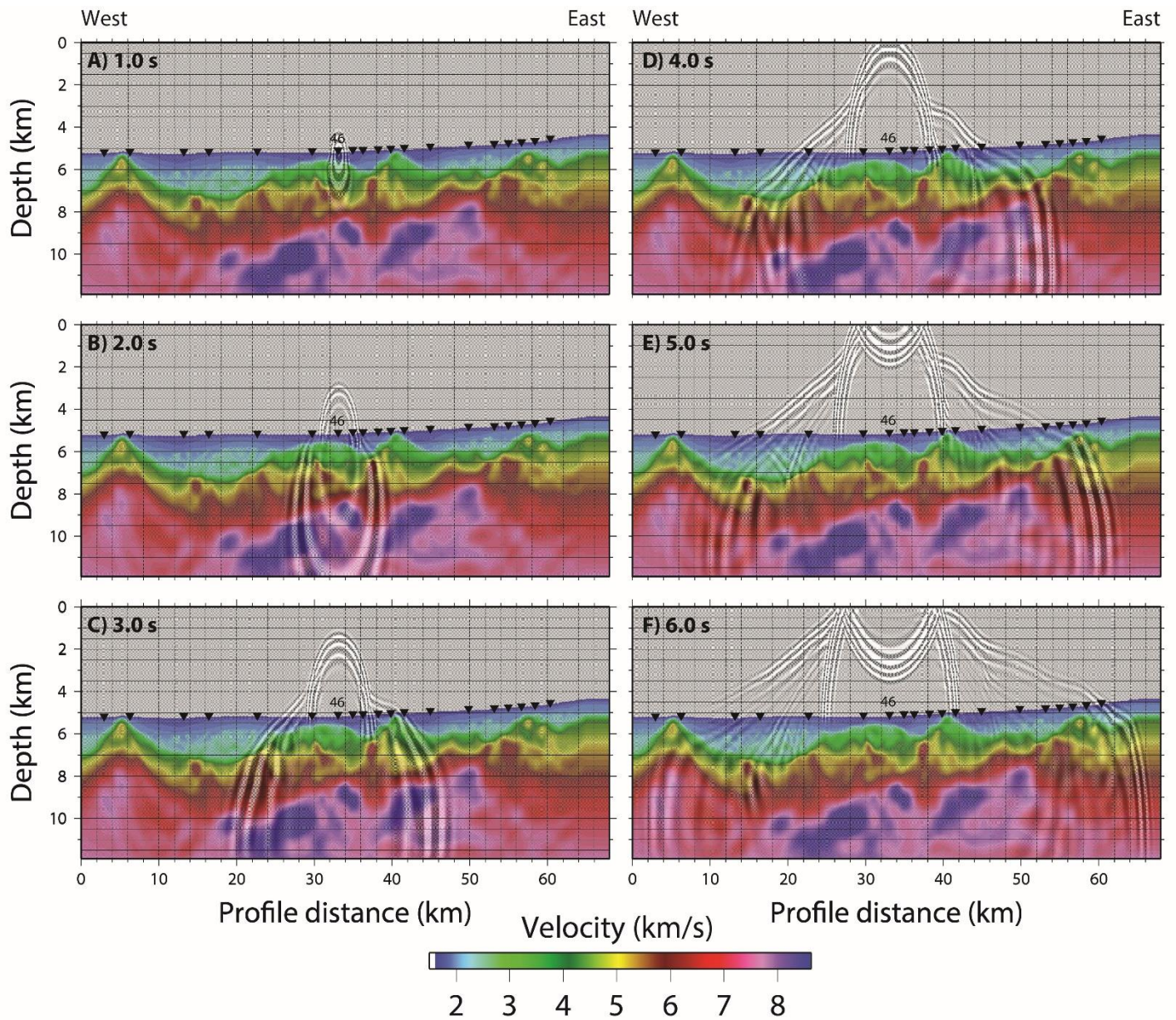
927 40, 50 and 60 km, respectively). Line colours are black: starting model, green: 1.0 s, yellow:

928 1.5 s, light blue: 2.0 s, blue: 2.5 s.

929

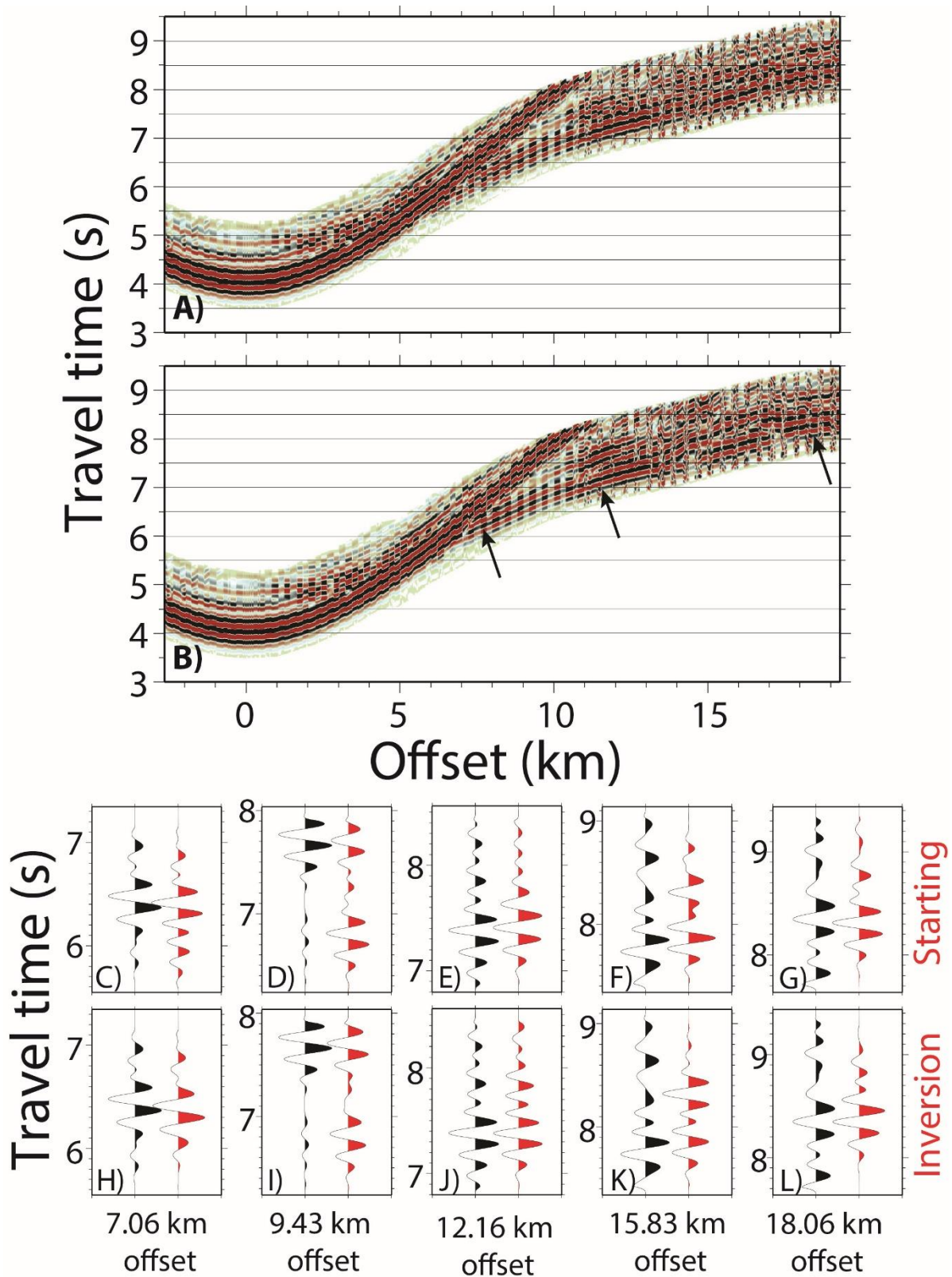


930 Figure 8: Inversion models for varying starting sediment velocity models, as described in
 931 section 3.7: A) High velocities B) Low velocities C) High-velocity gradient D) Low-velocity
 932 gradient. Black upturned triangles indicate the locations of utilised instruments, black dashed
 933 line indicates the base of post-rift sediments. Vertical exaggeration is 3.2. E-J) 1D velocity
 934 profiles through the resulting models, below post-rift sediment, at set profile distances (10,
 935 20, 30, 40, 50 and 60 km, respectively). Line colours are black: starting model, green: high
 936 velocities, yellow: low velocities, light blue: high-velocity gradient, blue: low-velocity
 937 gradient.

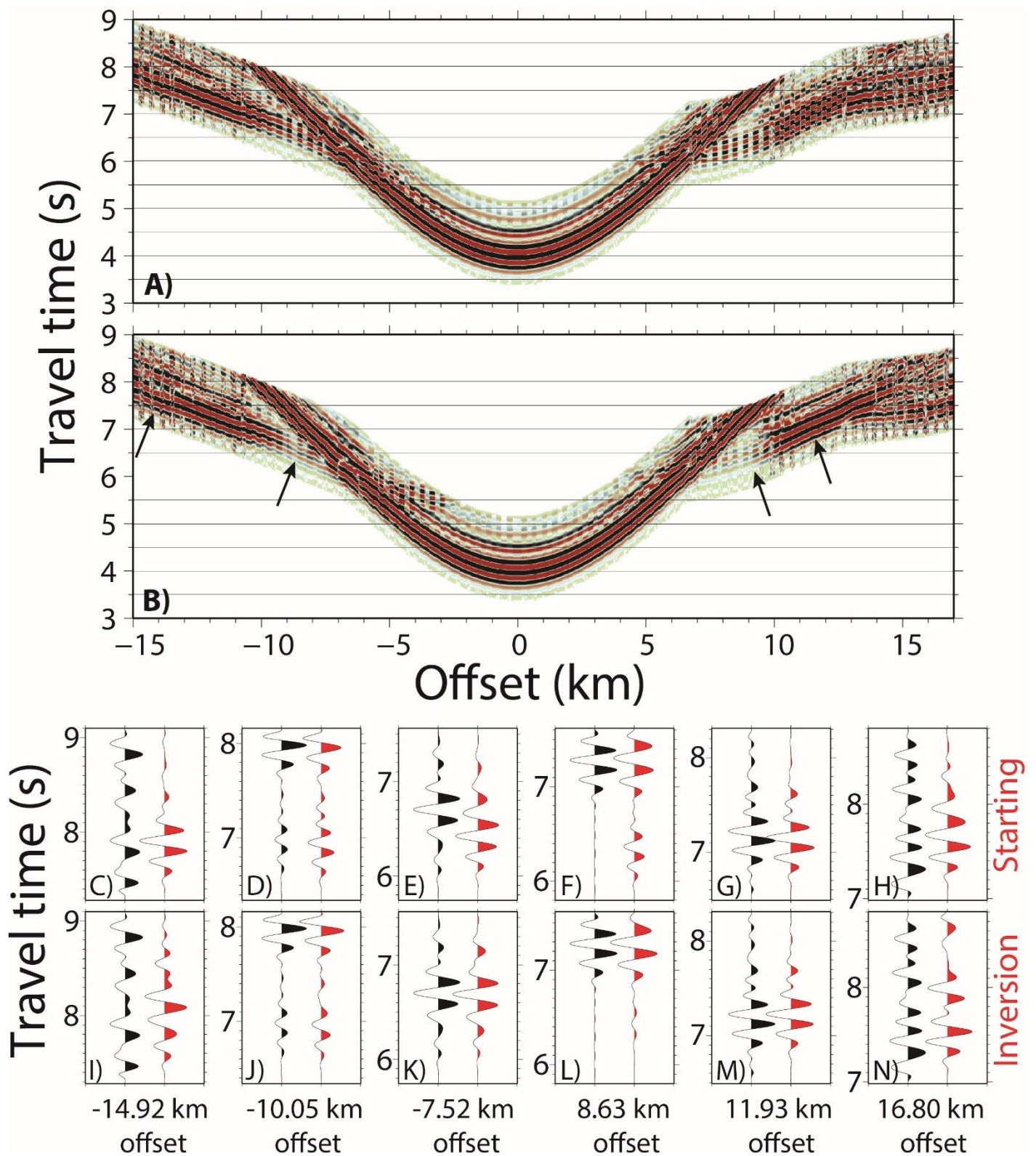


938 Figure 9: Propagation of the derived source wavelet through the final inversion model,
 939 originating at OBS46, at discrete times: A) 1.0 s, B) 2.0 s, C) 3.0 s, D) 4.0 s, E) 5.0 s, F) 6.0
 940 s. Black upturned triangles indicate the locations of utilised instruments. Vertical
 941 exaggeration is 3.2.

942

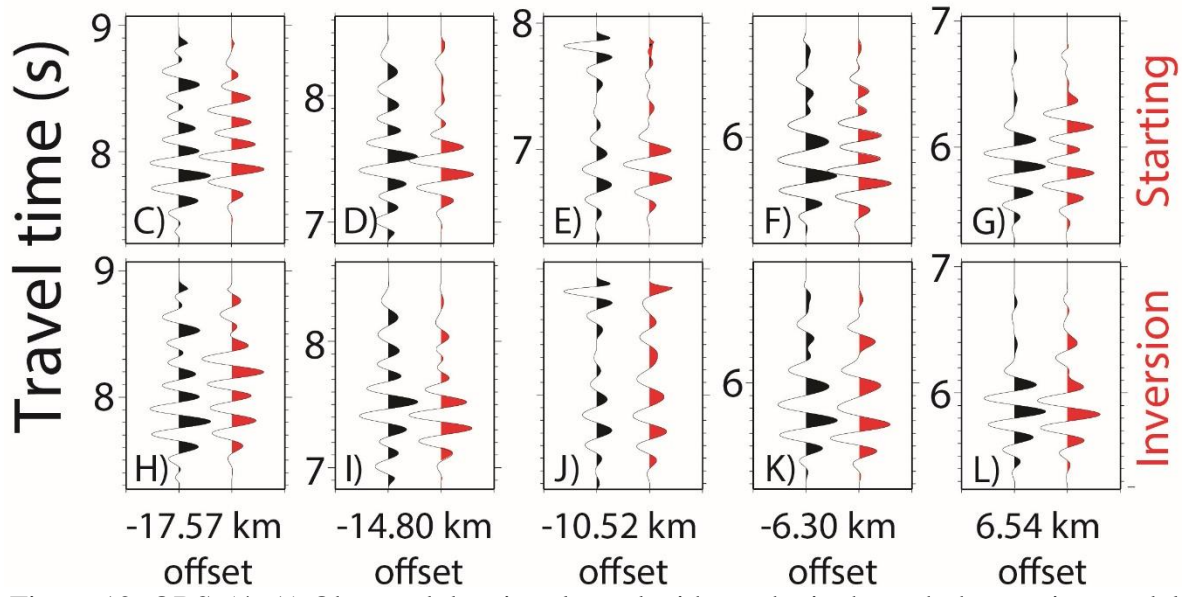
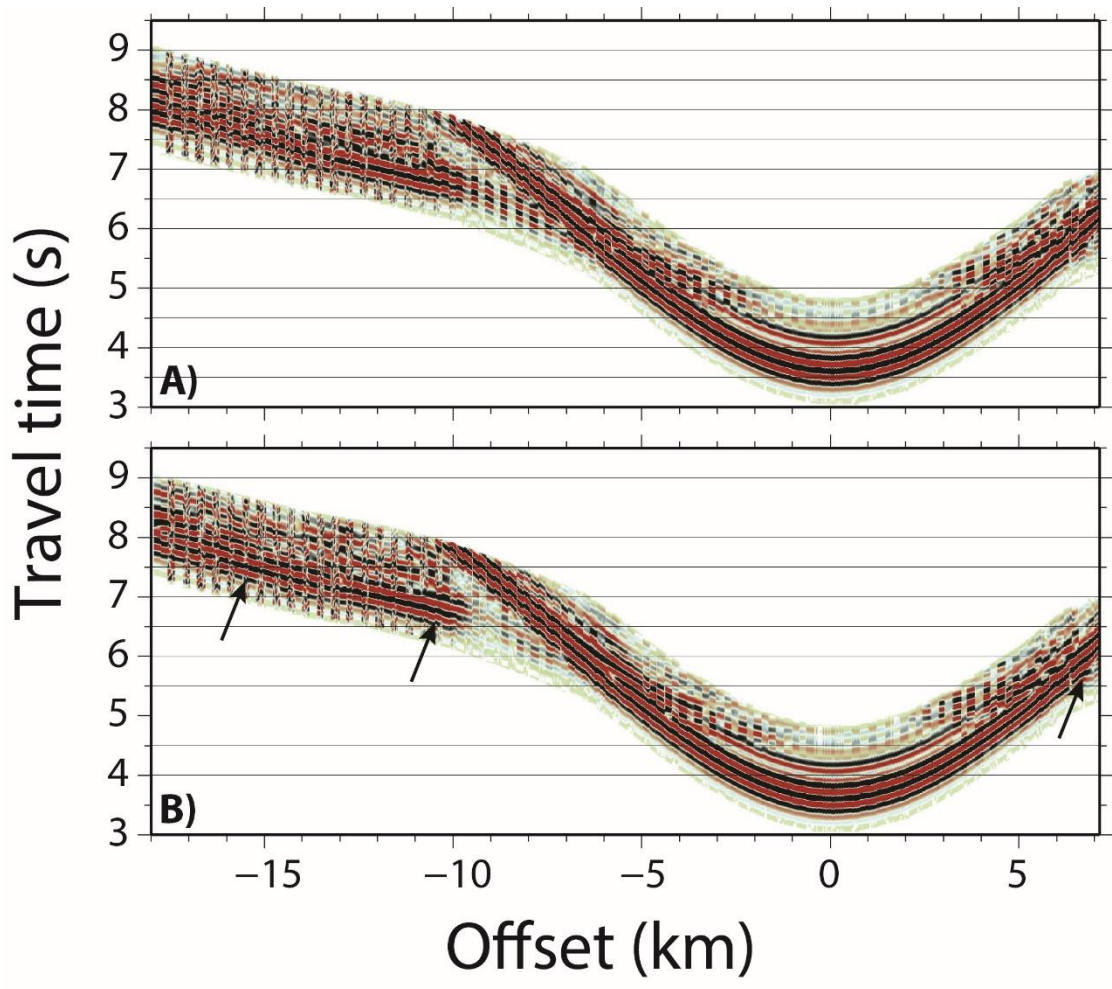


943 Figure 10: OBS 37. A) Observed data interleaved with synthetic through the starting model in
 944 alternative offset bins of 200 m. B) Observed data interleaved with synthetic through the
 945 inversion model in alternative offset bins of 200 m. C-G) Black traces: observed data, red
 946 traces: synthetic data through the starting model. H-L) Black traces: observed data, red traces:
 947 synthetic data through the FWI model.



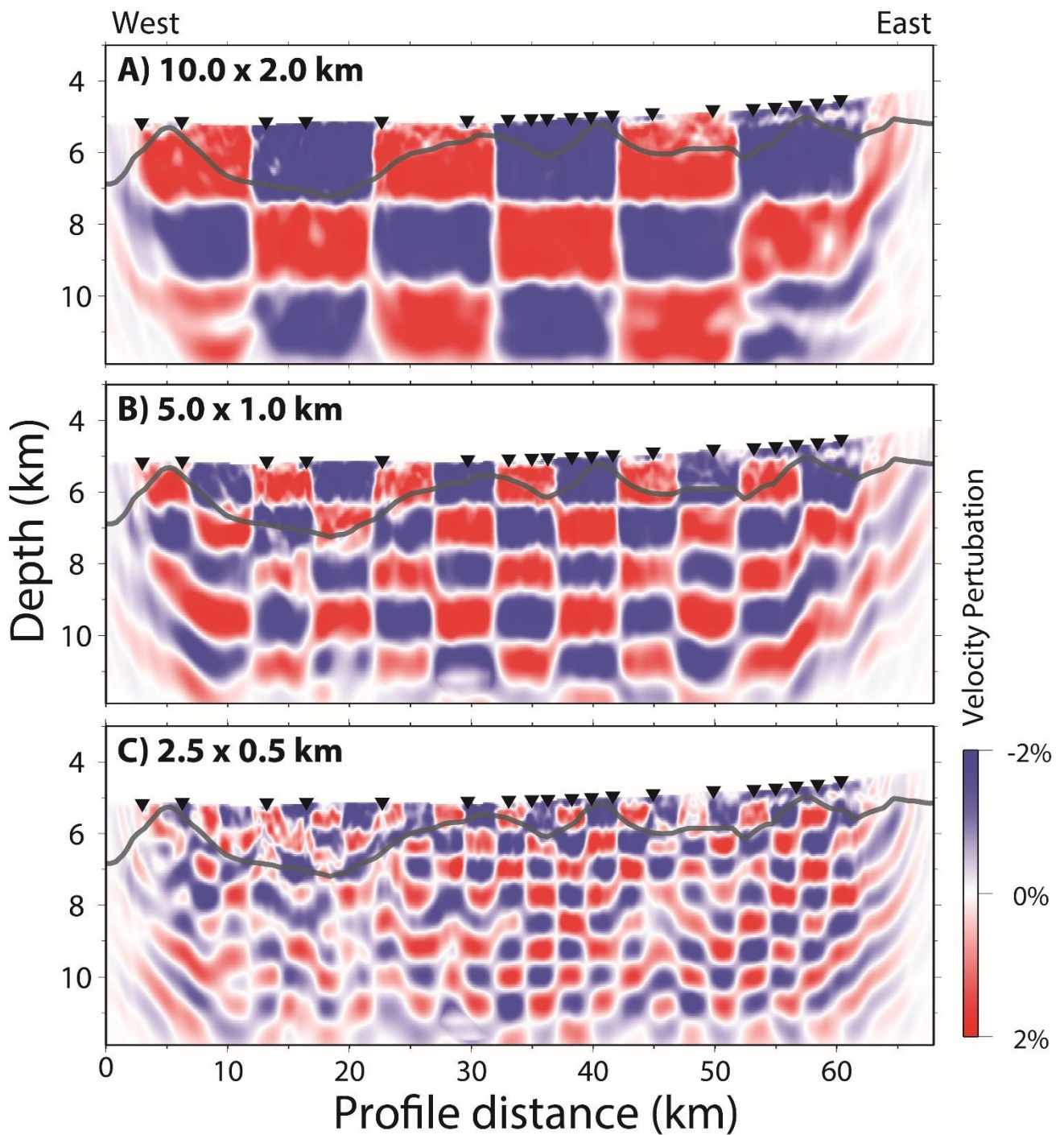
948 Figure 11: OBS 46. A) Observed data interleaved with synthetic through the starting model in
 949 alternative offset bins of 200 m. B) Observed data interleaved with synthetic through the
 950 inversion model in alternative offset bins of 200 m. C-H) Black traces: observed data, red
 951 traces: synthetic data through the starting model. I-N) Black traces: observed data, red traces:
 952 synthetic data through the FWI model.

953



954 Figure 12: OBS 54. A) Observed data interleaved with synthetic through the starting model in
 955 alternative offset bins of 200 m. B) Observed data interleaved with synthetic through the
 956 inversion model in alternative offset bins of 200 m. C-G) Black traces: observed data, red
 957 traces: synthetic data through the starting model. H-L) Black traces: observed data, red traces:
 958 synthetic data through the FWI model.

959

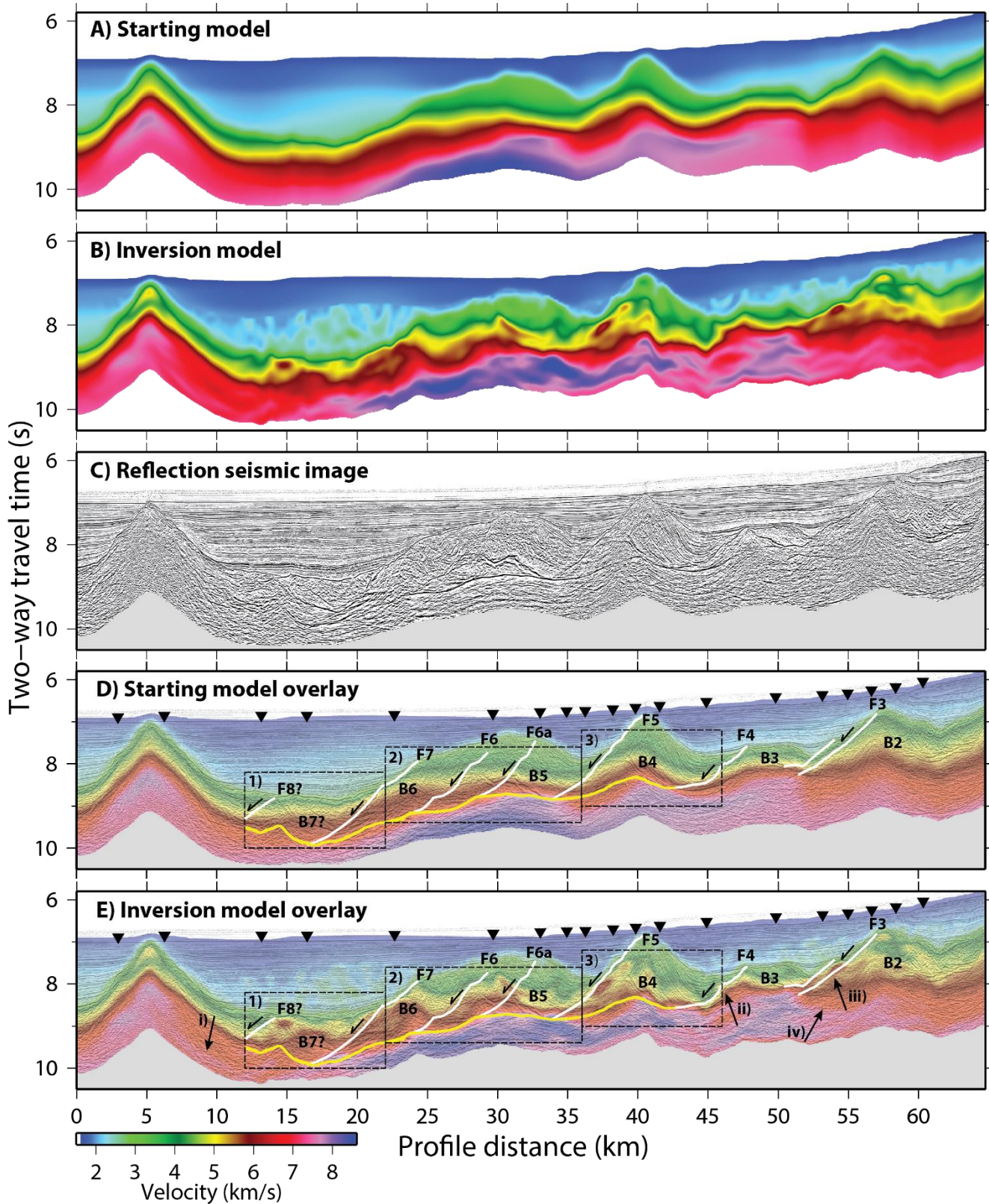


960

961 Figure 13: Checkerboard resolution test results. Anomaly check dimensions: A) 10.0 x 2.0
 962 km, B) 5.0 x 1.0 km, C) 2.0 x 0.5 km. Vertical exaggeration is 3.4. Grey line represents the
 963 top of the syn-rift sediments.

964

965



966 Figure 14: Comparison of large scale features with seismic reflection imaging. A) Starting
 967 velocity model B) Final FWI velocity model C) Kirchhoff pre-stack time-migrated
 968 multichannel seismic image of inline 420. D) Reflection image overlain with starting velocity
 969 model. E) Reflection image overlain with FWI velocity model. White lines indicate the
 970 location of interpreted normal faulting; the yellow line is the interpreted S reflector. Black

971 upturned triangles indicate the locations of utilised instruments. Dashed black rectangles
972 indicate the zoomed regions illustrated in Figure 4-15. Black arrows indicate regions
973 discussed in the text.

974

975

976

977

978

979

980

981

982

983

984

985
 986 Fig
 987 ure
 988 15:
 989 A-
 990 C)
 991 Sec
 992 tion
 993 s of
 994 inte
 995 rest
 996 of
 997 the
 998 Kir
 999 ch
 1000 off
 1001 pre-
 1002 stac
 1003 k
 1004 tim
 1005 e-
 1006 mig
 1007 rate
 1008 d
 51

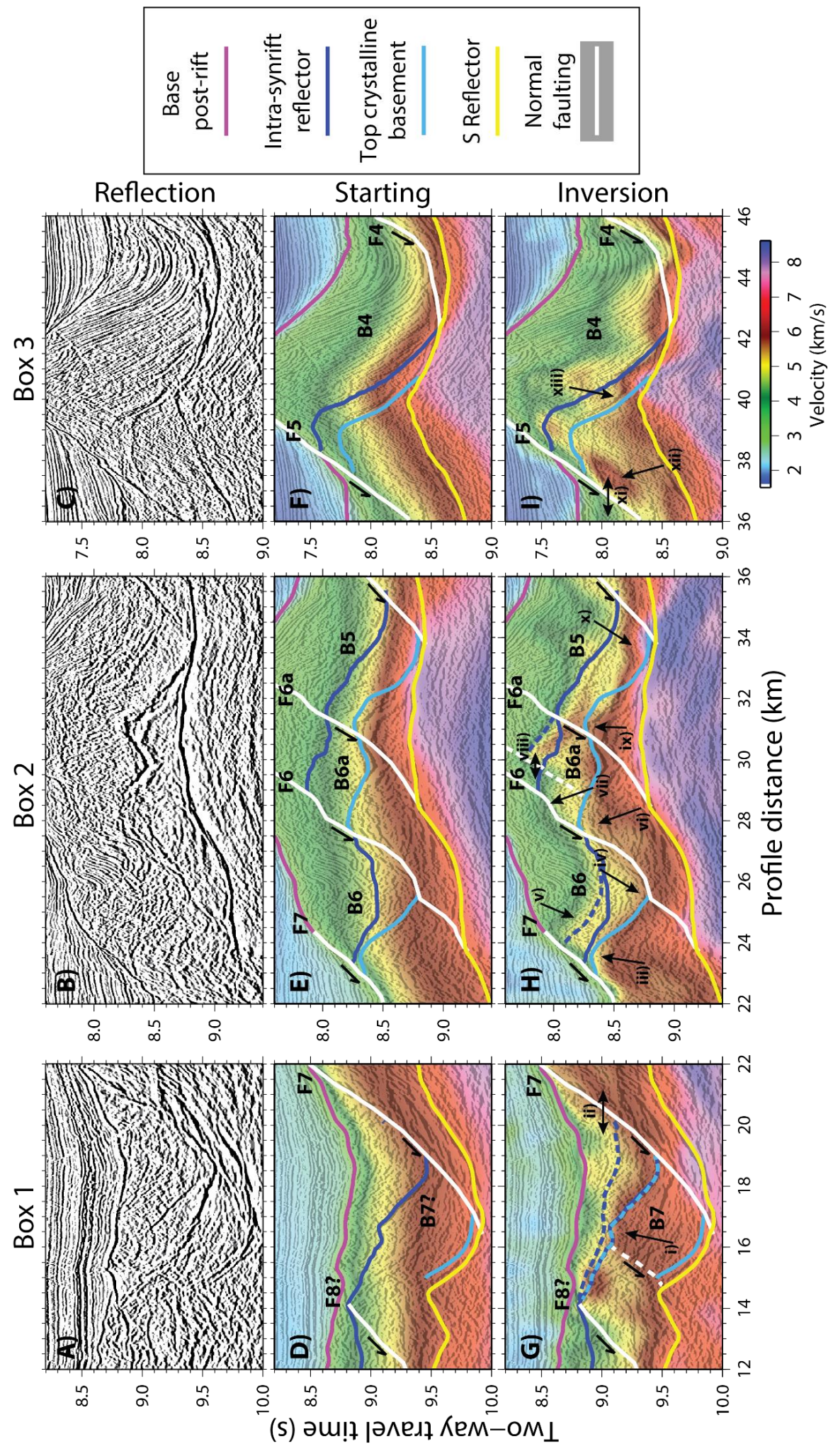


Figure 15: Caption on next page.

1009 multichannel seismic image of inline 420. D-C) Same reflection images as A-C, overlain by
1010 the time-converted starting velocity model. G-I) Same reflection images as A-C, overlain by
1011 the time-converted final FWI velocity model. Interpreted faults and horizons: white lines
1012 indicate normal faulting; yellow lines indicate the S-reflector; pink line indicate the base of
1013 the post-rift sediments; dark blue indicate an intra syn-rift horizon; light blue indicates the top
1014 of crystalline basement. Black arrows indicate regions discussed in the text. Dashed lines
1015 indicate the reinterpretation of faults and horizons, based on the final FWI velocity model.

1016

1017

1018

1019

1020

1021

1022

1023

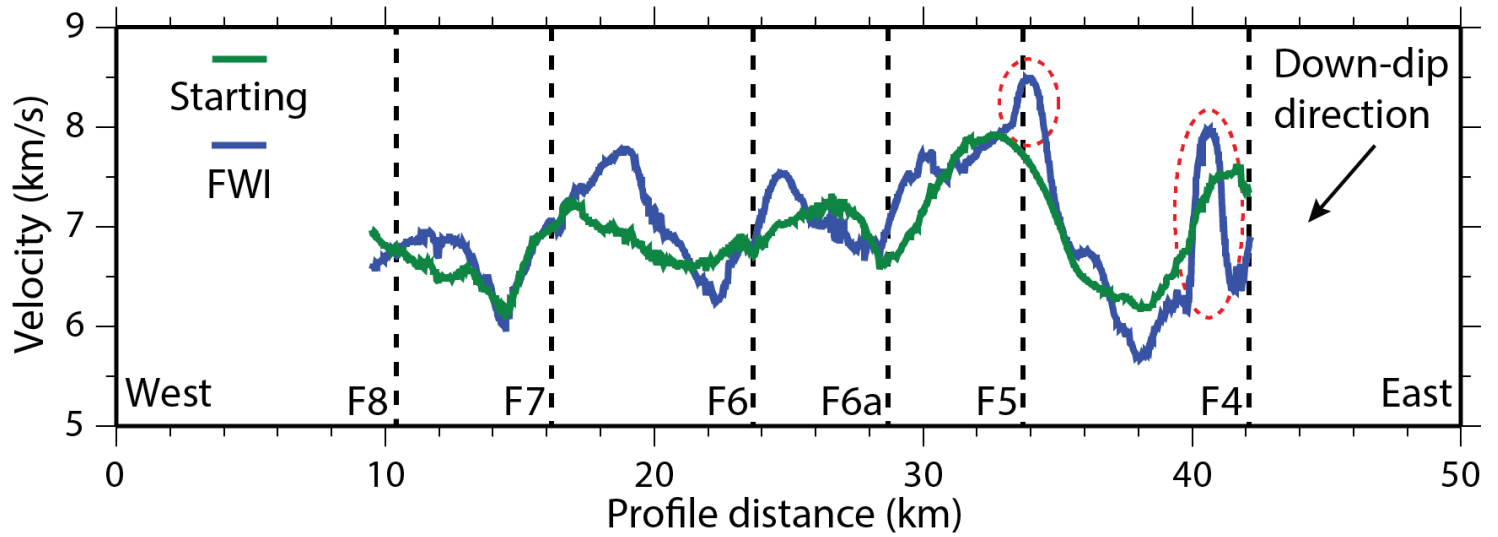
1024

1025

1026

1027

1028



1029

1030 Figure 16: Velocities below the interpreted S-reflector (averaged over a 100 ms window).

1031 The green line indicates velocities from the starting velocity model; the blue line indicates

1032 velocities from the final FWI velocity model. Vertical dashed lines indicate the locations

1033 where interpreted normal faults sole onto the S-reflector. Red dashed ellipses indicate

1034 anomalous features of the inversion model.